








# Let It Go: Geophysically Driven Ejection of the Haumea Family Members

Jessica L. Noviello<sup>1,2</sup> , Steven J. Desch<sup>3</sup> , Marc Neveu<sup>4,5</sup> , Benjamin C. N. Proudfoot<sup>6</sup> , and Sarah Sonnett<sup>7</sup> 

<sup>1</sup>NASA Postdoctoral Management Program Fellow, Oak Ridge Associated Universities, Oak Ridge, TN 37830, USA; [jessica.noviello@nasa.gov](mailto:jessica.noviello@nasa.gov)

<sup>2</sup>Planetary Systems Laboratory, NASA Goddard Space Flight Center, Greenbelt, MD 20771, USA

<sup>3</sup>School of Earth and Space Exploration, Arizona State University, PO Box 871404, Tempe, AZ 82587-1404, USA

<sup>4</sup>Department of Astronomy, University of Maryland, College Park MD, USA

<sup>5</sup>Planetary Environments Laboratory, NASA Goddard Space Flight Center, Greenbelt, MD 20771, USA

<sup>6</sup>Brigham Young University, Department of Physics and Astronomy, N283 ESC, Provo, UT 84602, USA

<sup>7</sup>Planetary Science Institute, Tucson, AZ 85719, USA

Received 2021 December 20; revised 2022 August 29; accepted 2022 August 29; published 2022 September 29

## Abstract

We present a new model for Haumea’s formation and evolution that relies on geophysical and geochemical data informed from observations of Haumea and meteorites to explain the characteristics of Haumea and its dynamical family. We hypothesize that after the impact of two partially differentiated Kuiper Belt objects, Haumea’s rocky core grew, decreasing its moment of inertia (MOI), spinning it up to the point that icy material was ejected from its surface. This ice, carrying about 3% of Haumea’s mass and 14% of its initial angular momentum, comprises the Haumean dynamical family and the ring system and moons observed today. Later, melted ice hydrated Haumea’s core and it grew, increasing Haumea’s MOI and spinning it down to the modern value. We use the geophysical code *kyushu* to demonstrate that solutions exist for a Haumea in hydrostatic equilibrium at each of these hypothesized stages. Geochemical modeling using the *IcyDwarf* code constrains the formation of Haumea’s core and the creation of the collision family to have occurred after roughly 150–160 Myr of solar system evolution ( $4.41 \pm 0.01$  Gyr ago). Hydration of the core was complete by about 0.20 Gyr, but a substantial subsurface ocean with half the mass of Earth’s oceans persisted until it froze at about 0.45 Gyr, making Haumea the solar system’s most distant potential relict ocean world.

*Unified Astronomy Thesaurus concepts:* [Kuiper belt \(893\)](#); [Dwarf planets \(419\)](#); [Planetary interior \(1248\)](#)

## 1. Introduction

The Kuiper Belt object (KBO) 2003 EL<sub>61</sub> Haumea is a puzzle of a world. Uniquely among large KBOs, it is almost uniformly (>90%) covered in water ice (Barkume et al. 2006; Pinilla-Alonso et al. 2009). There is evidence of an anomalous “red spot” that gives Haumea a longitudinally heterogeneous surface composition (Lacerda et al. 2008; Lockwood et al. 2014; Gougeot et al. 2016); this red spot has been interpreted as evidence of organics on Haumea’s surface. These variations cannot account for Haumea’s light curve, which shows marked variations in brightness of  $\approx 0.3$  mag as Haumea rapidly spins every  $3.91531 \pm 0.00005$  hr (Rabinowitz et al. 2006; Lellouch et al. 2010; Lockwood et al. 2014), the fastest rotation rate of any large object in the solar system. The variations instead have been interpreted as Haumea having a triaxial ellipsoid ( $a > b > c$ ) shape, with the  $b/a$  axis ratio estimated to be between 0.77 and 0.87 (Lacerda & Jewitt 2007; Lockwood et al. 2014). Haumea possesses two moons, Nāmaka and (more distant) Hi’iaka (Ragozzine & Brown 2009), which has allowed an estimate of Haumea’s mass,  $4.006 \times 10^{21}$  kg (Ragozzine & Brown 2009). Haumea also possesses a ring, discovered during an occultation (Ortiz et al. 2017). The occultation event has allowed refined estimates of Haumea’s size, with semiaxes  $a = 1050$ ,  $b = 840$ , and  $c = 537$  km apparently most consistent with the observations (Dunham et al. 2019).

A recent debate has centered on whether Haumea could be a fluid body in hydrostatic equilibrium, or whether it must support

internal shear stresses. Haumea is large enough that it should behave as a fluid, and indeed, the earliest light-curve analyses indicated that Haumea’s shape was consistent with a Jacobi ellipsoid with semiaxes of  $980 \times 759 \times 498$  km and a uniform density of  $\approx 2600$  kg m<sup>-3</sup> (Rabinowitz et al. 2006). Jacobi ellipsoid solutions presume a uniform density, so this model would demand that Haumea is mostly hydrated silicate, with a thin veneer of water ice to explain its surface reflectance. To the extent that ice comprises a significant fraction of Haumea’s mass, it must deviate from a Jacobi ellipsoid. Ortiz et al. (2017) inferred from Haumea’s occultation shadow semiaxes of  $1161 \times 852 \times 513$  km and an average density of  $\approx 1885$  kg m<sup>-3</sup>. This would demand that Haumea’s internal composition support shear stresses, e.g., as a granular fluid (Holsapple 2001). Likewise, under the unjustified assumption that layers within Haumea must conform to confocal ellipsoids, Kondratyev (2016) also inferred a structure for Haumea inconsistent with a shearless fluid. The differing interpretations have been resolved by Dunham et al. (2019), who modeled the internal structure of a differentiated (rocky core, icy mantle) Haumea using the *kyushu* code they wrote to calculate the gravitational potential. Assuming a mantle of pure water ice, they found Haumea to be consistent with semiaxes of  $1050 \times 840 \times 537$  km, an average density of  $2018$  kg m<sup>-3</sup>, and a rocky core with a density of  $2680$  kg m<sup>-3</sup> comprising 83% of Haumea’s mass. A shearless fluid in such a configuration, Dunham et al. (2019) showed, would be in hydrostatic equilibrium at the high spin rate experienced by Haumea.

Haumea is also unique among KBOs because it is part of a dynamical family, the only one known in the Kuiper Belt (Brown et al. 2007). The Haumeans, as the family members are collectively called here, all have water ice-rich surfaces and are



Original content from this work may be used under the terms of the [Creative Commons Attribution 4.0 licence](#). Any further distribution of this work must maintain attribution to the author(s) and the title of the work, journal citation and DOI.

dynamically linked by their relatively low dispersion velocities of  $<150 \text{ m s}^{-1}$  (relative to the osculating orbital elements of the centroid; Volk & Malhotra 2012). When discovered, it was presumed that the Haumeans were ejected by a collision that would have also stripped Haumea’s ice mantle, leading to its high average density, and increased its spin rate to the high value seen today (Brown et al. 2007). This idea has lost support, as it left unexplained several curious facts. First, the total mass of the Haumeans (including Haumea’s moons) is not large enough to account for the total amount of ice presumably lost during the collision. The family members comprise only  $\approx 3\%$  of Haumea’s total mass (Pike et al. 2020). Hi’iaka and Nāmakā comprise an estimated mass of 0.5% of Haumea’s total mass (Ragozzine & Brown 2009). Even with generous assumptions, the initial ice mass fraction of Haumea would not seem to exceed about 25%, which is curiously low.

Second, the family members appear to have anomalously low dispersion velocities. Typical dispersion velocities of family members in collisional families in the asteroid belt are on the order of the escape velocity (Benz & Asphaug 1999), which for Haumea is  $\approx 800 \text{ m s}^{-1}$ , considerably larger. However, this only takes into account the largest fragments. Later analyses found that the majority of particles in collisions are ejected with speeds a few times the escape velocity (Leinhardt & Stewart 2012). In Haumea’s case, this makes the mismatch between impact models and the observations more extreme.

Third, the orbital elements are not completely consistent with ejection of material along a plane (Proudfoot & Ragozzine 2019), such as might arise after a low-velocity “graze-and-merge” collision, as advocated by Leinhardt et al. (2010), in which the postimpact body is left with high angular momentum and basically undergoes rotational fission. While Haumea’s high spin rate seems consistent with a giant impact, the creation of the Haumeans appears to be decoupled from this event.

The odd combination of Haumea family characteristics makes it difficult for a single formation model to explain all of its elements. While all models begin with an initial impact event that gave Haumea its fast spin rate, the details beyond this step are unclear. A single large impact event as presented by Brown et al. (2007) and Ragozzine & Brown (2007) proposes that proto-Haumea collided with a similarly sized object that stripped off its ice mantle. The ejected mantle material became the Haumeans. This model successfully explains Haumea’s rapid spin rate and the spectral similarities among the Haumeans but struggles to explain the small velocity dispersion of the family members and their overall orbital elements. Another model by Schlichting & Sari (2009) proposed that after the large impact event, the material ejected from proto-Haumea reaggregated into a single large ( $R \sim 260 \text{ km}$ ) satellite. The satellite then underwent tidal migration away from Haumea, whereupon it experienced another catastrophic impact. Most of the material left the system, but two main pieces remained that became the moons Hi’iaka and Nāmakā. The satellite disruption model explains Haumea’s rapid spin rate, the spectral similarities of the Haumeans, and the relatively small velocity dispersion but struggles to explain the orbital elements of the Haumeans and the relationship between the number, size, and velocity of the Haumeans (Proudfoot & Ragozzine 2019). The collision that destroyed the satellite is very unlikely to happen given a modern Kuiper Belt configuration ( $\sim 10^{-3}$ ), so it must have happened prior to the excitation of the Kuiper Belt. Within this context,

Schlichting & Sari (2009) estimated that the probability of an event described in this model is 10% over the age of the solar system. The last primary model is the graze-and-merge model (Leinhardt et al. 2010). In this scenario, Haumea was impacted by a similarly sized object that remained gravitationally bound to, and eventually reimpacted and merged with, proto-Haumea. The system acquired such a rapid spin rate that material was spun off of the longest axis. The material eventually reaccreted into the Haumeans and the ring system observed today. Ortiz et al. (2012) similarly proposed that the family members and satellites were created by rotational fission. This model successfully explains the spectral similarities of the Haumeans, Haumea’s rapid spin rate, and the number–size–velocity relation of the Haumeans but does not explain the orbital elements of the Haumeans (Proudfoot & Ragozzine 2019).

Here we present a new hypothesis for the formation of the Haumeans, depicted as six stages in Figure 1. In stages 1 and 2, it is supposed that two similarly sized, partially differentiated KBOs in the classical Kuiper Belt collided obliquely in the graze-and-merge scenario of Leinhardt et al. (2010). We hypothesize that the collision would have taken place as a result of Neptune’s migration through the primordial Kuiper Belt as part of a Nice model–like dynamical instability (Tsiganis et al. 2005) but before Neptune completed its outward migration, so that any bodies ejected during this stage would not have retained coherent orbital elements and therefore cannot be identified today as family members. We also hypothesize that the impact occurred at a special time in the bodies’ evolution; they had begun to differentiate, forming a rocky core and icy mantle, beneath an undifferentiated rock–ice crust, but they had only partially (perhaps 20%) differentiated. After the impact, we hypothesize that Haumea would have had about 1.03 times the mass of present-day Haumea ( $M_{\text{H}}$ ), or  $M = 1.03 M_{\text{H}}$ , and 1.14 times the angular momentum of present-day Haumea ( $J_{\text{H}}$ ), or  $J = 1.14 J_{\text{H}}$ . Haumea would have started out as a primarily undifferentiated rock–ice mixture with a small rocky core at its center and a small amount of water ice on its surface.

In stages 3 and 4, the postimpact Haumea differentiated. As Haumea heated and more rocky material settled through the mantle to enlarge its core, this would have decreased its moment of inertia (MOI) and (conserving angular momentum) increased its spin rate. At the culmination of core formation, a “pre-fling” Haumea would have spun up to the point that some icy material on its equator was flung off, most likely going into orbit around Haumea and eventually forming the ring, moons, and moonlets. Mutual scattering of these moonlets led most of them to leave the Haumea system altogether, forming the Haumea family. This material would have removed both mass and angular momentum, eventually leaving it with  $M = 1.00 M_{\text{H}}$  and  $J = 1.00 J_{\text{H}}$ . It is presumed that the ejection of the Haumeans took place after Neptune’s migration, so that the icy fragments flung off in this stage would largely remain a coherent dynamical family.

After ejection of the icy material from the equator, during stage 5, the “post-fling” Haumea would have evolved further, as ice melted and water reacted with the rocky core, serpentinizing it. This would have led to a larger core of lower-density hydrated silicate, at the expense of a smaller ice mantle. While retaining a mass  $M = 1.00 M_{\text{H}}$  and angular momentum  $J = 1.00 J_{\text{H}}$ , the larger MOI would have decreased its spin rate to the value observed today, leaving the modern-day Haumea (stage 6).

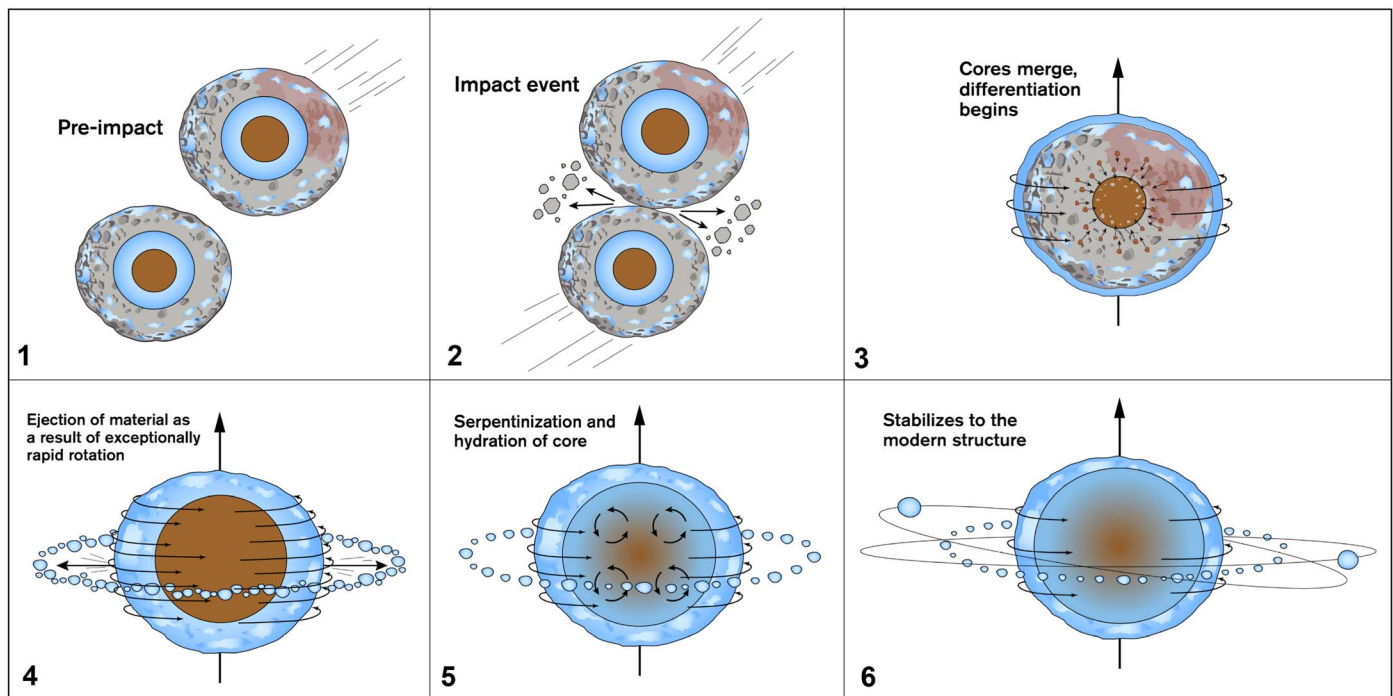


**Figure 1.** Stages in our hypothesized evolution of Haumea. In stage 1, two similar KBOs have partially differentiated and have small rock cores and ice mantles underneath undifferentiated rock/ice. In stage 2, the bodies collide in a graze-and-merge type collision, shedding rock/ice material that is lost. In stage 3, radiogenic heating drives further differentiation, which reduces Haumea’s MOI, spinning it up. In stage 4, during the final formation of the core, the spin rate is sufficient to eject material from the long axis of Haumea, forming a disk of icy material. The loss of angular momentum slows Haumea’s spin, and in stage 5, the hydration and swelling of the core increase Haumea’s MOI and slow its spin rate further. Icy moonlets formed in the disk are lost as family members. Modern Haumea in stage 6 retains two large moons and a thin ring and is characterized by an ice mantle overlying a large rocky core of mostly hydrated silicate. Image credit: Sue Selkirk, ASU.

In this model, the ejection of the Haumeans is decoupled from the impact event, potentially explaining the low amount of mass that was ejected, as well as the low dispersion velocities of the ejected bodies. Although a giant impact was first inferred from the existence of the dynamical family, which was considered a collisional family like those in the asteroid belt (Brown et al. 2007), we consider it unlikely that material ejected during the giant impact could be identified as part of a family. First, most material escaping the system comes from the surfaces of the impactors, which are generally undifferentiated rock–ice mixtures. Leinhardt et al. (2010) assumed the surface would be ice, but Haumea and its family are unique in the Kuiper Belt for having nearly pure water-ice surfaces. The ejected objects would appear spectrally like other KBOs, unlike the spectrally distinct Haumeans. Second, for the reasons discussed in Section 5.2.1, the collision is much more likely to take place before the dynamical instability associated with Neptune’s migration (e.g., the Nice model of Tsiganis et al. 2005). Objects ejected during this time would not, however, retain their dynamic coherence (Levison et al. 2008). Third, if the simulations of Leinhardt et al. (2010) are representative, the mass of the ejected objects,  $\approx 6\%$  of Haumea’s mass, appears somewhat larger than the apparent mass of the family members,  $\approx 2\%–5\%$  of Haumea’s mass (Pike et al. 2020), suggesting that the dynamical family is distinct from an earlier collisional family.

Rotational fission appears to be a common mechanism for ejecting material, especially from small bodies spun up by the YORP effect, as with the object P/2013 R3 (Jewitt et al. 2010). If our model is demonstrated to be valid, Haumea would represent the first and perhaps only example of a dynamical family generated by rotational spin-up caused by a geophysical driven process.

The outline of this paper is as follows. In Section 2, we describe the *kyushu* code (Dunham et al. 2019) used to run the geophysical models, including the physics it employs and the computational uncertainties. In Section 3, we describe the different stages of Haumea’s evolution in our hypothesis, using the *kyushu* code to test whether hydrostatic equilibrium solutions exist at each stage. We begin with potential solutions for its modern state before resetting to the time immediately after the initial impact event, moving forward in time from there. In Section 4, we present calculations of Haumea’s thermal evolution after the giant impact using the *IcyDwarf* code (Neveu et al. 2015a). We use this to constrain the times at which various events, such as the onset of differentiation and any subsequent interior hydration events, in Haumea’s evolution must occur. In Section 5, we discuss the implications of this work for Haumea’s potential core and mantle composition and the overall timing of key events on the outer solar system’s evolution, including timelines for the differentiation of other planetary bodies. We also discuss the dynamics of the Haumea family, how the dynamics of the model we propose align with observations, and the effects of observational uncertainties on our model. In Section 6, we summarize our hypothesis and the work done to support it detailed in this paper and present a succinct timeline for Haumea’s history. We conclude with connecting this study of Haumea to the search for life in the outer solar system and the exploration of ocean worlds.

## 2. Methods

To test whether Haumea’s interior structure would be consistent with the evolutionary sequence outlined above, we must calculate the internal distributions of material inside a

rapidly rotating, differentiated body composed of two shearless fluids in hydrostatic equilibrium. To do this, we employ the `kyushu` code written by Dunham et al. (2019), which is itself based on the algorithms of Hachisu (1986a, 1986b). A similar code was written by Price & Rogers (2020) to study metal-rich exoplanets. Unlike their code, we do not assume a compressible equation of state, allowing material to have density  $\rho_m$  if it is in the mantle at pressures  $P < P_{\text{CMB}}$ , the core–mantle boundary pressure, or density  $\rho_c$  if it is in the core at pressures  $P > P_{\text{CMB}}$ . This is appropriate for Haumea because the bulk modulus of planetary materials is typically tens of GPa, whereas the peak pressures inside Haumea are  $<0.4$  GPa, justifying our neglect of compressibility.

The `kyushu` code is a finite-element code with uniform density within zones defined on a spherical grid. The grid typically assumes  $N_r = 201$  values of  $r$  between zero and  $R = 1200$  km, inclusive;  $N_\mu = 17$  values of  $\mu = \cos\theta$  between zero and 1, inclusive; and  $N_\phi = 17$  values of  $\phi$  between zero and  $\pi/2$ , inclusive. This involves a total of 51,200 grid zones per simulation. Symmetry is assumed across the  $x$ – $y$  plane, and  $m = 2$  axisymmetry is assumed, allowing for (but not imposing) a triaxial ellipsoid shape. The code calculates the gravitational potential  $\Phi$  corresponding to this configuration using an expansion in spherical harmonics, using  $N_l = 16$  terms. From the Bernoulli equation, it is known that

$$\int \rho^{-1} dP - \omega^2 r_\perp + \Phi = C, \quad (1)$$

where the first term is the enthalpy,  $H$ ; the second term is the centrifugal potential, with  $r_\perp = (x^2 + y^2)^{1/2}$ ; and  $C$  is a constant. On the tips of the  $a$ - and  $b$ -axes,  $H = 0$ , and the code calculates the only values of the constant  $C$  and the rotation rate  $\omega$  that allow the above equation to be satisfied at those two points. For the given mass distribution and potential  $\Phi$  and constant  $C$ , the code calculates  $H$  at each location and inverts it to find the pressure there, then uses our simplified equation of state to set the density in that zone. The mass distribution and  $\Phi$  are updated, and the code is run to convergence. The code is then run iteratively until solutions are found that conform to a total given mass  $M$  and spin period  $P$ .

Inputs of the code include the semiaxes,  $a$  and  $b$ ; the mantle density,  $\rho_m$ ; and the total mass of the system,  $M$ . Outputs of the code include the semiaxis,  $c$ ; inputs to the equation of state, namely the core density,  $\rho_c$ , and the core–mantle boundary pressure,  $P_{\text{CMB}}$ ; the density at all locations; and the angular velocity  $\omega$ , or spin period  $P$ . From these outputs, we can test whether the distributions conform to a triaxial ellipsoid; if the core does conform, we can define  $a_c$ ,  $b_c$ , and  $c_c$  and calculate the core mass,  $M_c$ . Although a triaxial ellipsoid distribution was not imposed, in practice, we have never found a solution for either the core–mantle boundary or the outer surface that deviated from a triaxial ellipsoid by more than the spatial resolution of the grid. We could numerically integrate the density distribution to derive the MOI,  $I$ , and therefore the total angular momentum,  $J = I\Omega$ ; but in practice, it introduces less uncertainty to assume triaxial ellipsoid shapes for the core and outer surface and use analytical formulae (Equation (2)). In practice, we seek families of solutions that conform to a given spin period  $P$  or angular momentum  $J$ , varying only  $\rho_m$  for fixed  $a$  and  $b$  (or varying only  $a$  and  $b$  for fixed  $\rho_m$ ).

Several tests were conducted to test the accuracy of the code. As described by Dunham et al. (2019), the code has been

benchmarked against analytical formulae by selecting  $a$  and  $b$ ,  $M$ , and  $\omega$  known to represent Jacobi ellipsoids; the code returned the correct values for  $c$  and  $\rho$  corresponding to the Jacobi ellipsoid to within  $<1\%$ . The runs conducted here generally used a spatial resolution coarser than those of Dunham et al. (2019) by a factor of 2 (50,000 zones instead of 400,000 zones). Nevertheless, the values of key metrics generally agreed with their results to within  $<1\%$ .

We ran the code at different numerical resolutions, conducting convergence tests. Based on these, we estimate the following uncertainties in different values. The  $P$  is accurate to within  $\pm 0.03$  hr ( $<0.8\%$ ). The mass  $M$  is matched to the target mass (1.00 or  $1.03 M_{\text{H}}$ ) to arbitrary accuracy, typically  $\ll 1\%$ . The semiaxes  $a$  and  $b$  are fixed quantities, and  $c$  is accurate to within about  $\pm 0.1$  km ( $<0.02\%$ ). To the extent that the outer boundary is a triaxial ellipsoid, the average density  $\rho_{\text{avg}}$  is constrained with high accuracy, but the assumption of a triaxial ellipsoid cannot be tested to better than the spatial resolution of the code, which is roughly half the width of a radial zone (1200 km/200), or about  $\pm 3$  km or  $<0.4\%$ . Likewise, the semiaxes of the core are  $c$ ,  $a_c$ ,  $b_c$ , and  $c_c$  and accurate to within  $\pm 3$  km ( $<0.6\%$ ), so the core volume is not accurate to better than about 2%. From our own convergence studies, the density of the core,  $\rho_c$ , is accurate to within  $\pm 70$  kg m $^{-3}$ , or about  $<2\%$ . Combined, the core mass  $M_c$  is by far the most uncertain quantity, known only to within about 3%. We found that it is more accurate to calculate  $J$  from derived quantities, rather than integration over cells, but it is also uncertain to within about 2%–3%.

### 3. Haumea’s Evolution

#### 3.1. Modern-day Haumea

Although it is the last stage in Haumea’s evolutionary sequence, we begin our calculations with an evaluation of modern-day (stage 4) Haumea’s interior to constrain the present-day angular momentum,  $J_{\text{H}}$ . The MOI  $I$  of a triaxial ellipsoid of homogeneous density, rotating about the  $c$ -axis, is given by  $I = M(a^2 + b^2)/5$ . For now, we assume that Haumea is divided into a core of uniform density  $\rho_c$  and a mantle of uniform density  $\rho_m$ . Later (Section 5.1), we will investigate the effect on  $I$  of having the core divided into two zones with different densities. A finding of the calculations we perform is that the core–mantle boundary is well described as a triaxial ellipsoid of semiaxes  $a_c$ ,  $b_c$ , and  $c_c$ , and that the outer boundary is well described as a triaxial ellipsoid of semiaxes  $a$ ,  $b$ , and  $c$ . The two triaxial ellipsoids are aligned. This gives the core a mass  $M_c = 4\pi a_c b_c c_c \rho_c / 3$ . It is straightforward to show that the MOI of this two-layer configuration is

$$I = \frac{1}{5} \frac{\rho_m}{\rho_{\text{avg}}} M(a^2 + b^2) + \frac{1}{5} \frac{\rho_c - \rho_m}{\rho_c} M_c(a_c^2 + b_c^2), \quad (2)$$

where  $\rho_{\text{avg}}$  is the average density of Haumea. Multiplying  $I$  by the angular velocity  $\omega = 2\pi/P$ , where  $P = 3.915$  hr is the modern spin period, yields the angular momentum of Haumea,  $J = I\omega$ . As an aside, the MOI  $I$  can be divided by  $M_{ab}$  to yield

an MOI factor (MOIF):

$$\text{MOIF} = \frac{1}{5} \frac{\rho_m}{\rho_{\text{avg}}} \frac{a^2 + b^2}{ab} + \frac{1}{5} \frac{\rho_c - \rho_m}{\rho_c} \frac{M_c}{M} \frac{a_c^2 + b_c^2}{ab}. \quad (3)$$

In the limit of homogeneous density ( $\rho_m = \rho_c = \rho_{\text{avg}}$ ), this approaches  $(2/5)(a^2 + b^2)/(2ab)$ . This equals  $2/5$  if  $a = b$  (oblate spheroid) but generally exceeds  $2/5$  for  $b < a$ . Because the MOI and angular momentum are sensitive to the internal structure, we must use the *kyushu* code to calculate quantities (core size and density, overall average density) that correspond to fluid solutions in hydrostatic equilibrium. In practice, we calculate families of possible solutions for modern-day Haumea that match its present mass,  $M_H = 4.006 \times 10^{21}$  kg, and spin period,  $P = 3.915$  hr, inputting the semiaxes  $a$  and  $b$  and mantle density  $\rho_m$ . Once these quantities are fixed, they uniquely determine the other quantities of interest, including  $c$ ; the core semiaxes  $a_c$ ,  $b_c$ , and  $c_c$ ; and the core density  $\rho_c$ .

We explored a range of values for  $a$  and  $b$ , with full results presented in the [Appendix](#). For the purposes of the calculations presented here, we favored certain fixed values of the semiaxes  $a$  and  $b$ , driven by the need to match the light curve and occultation observations. Following the discussion of Dunham et al. (2019), we infer an axis ratio  $b/a = 0.80$  to match the amplitude of the light curve variations. We also attempt to match the size of Haumea's shadow, measured by Ortiz et al. (2017) during the occultation to be an ellipse on the plane of the sky with semiaxes  $(852 \pm 2) \times (569 \pm 13)$  km. Again following the discussion by Dunham et al. (2019), we fix Haumea's pole to be tilted with respect to the plane of the sky by  $13^\circ.7$  ( $\theta = 76^\circ.3$ ) and assume a rotational phase of about  $\psi = 13^\circ.3$ . The only values of  $a$  that are consistent with these parameters are  $a \approx 1054.1 \pm 2.5$  km. For the sake of setting up a reasonable grid in *kyushu*, we fixed  $a = 1056$  and  $b = 840$  km, which yields  $b/a = 0.795$ , very similar to the values  $a = 1050$  km,  $b = 840$  km, and  $b/a = 0.800$  chosen by Dunham et al. (2019). Our chosen values yield semiaxes of the shadow ellipse of  $853.5 \times 576.5$  km, completely consistent with Haumea's shadow size. They are similar to the values inferred by Kondratyev & Kornoukhov (2018).

Having fixed  $a$  and  $b$ , we then systematically varied  $\rho_m$  between 921 (pure water ice) and  $1600 \text{ kg m}^{-3}$  to reflect mantle compositions with varying water–rock ratios. The results are compiled in Table 1 and Figures 2 and 3. The solutions all match Haumea's mass,  $M = M_H = 4.006 \times 10^{21}$  kg, identically. They are selected to have period  $P = 3.915$  hr, and all do to within  $<1\%$ . Each solution has fixed  $a = 1056$  and  $b = 840$  km, and for the range of  $\rho_m$  considered,  $c$  varies from 537 to  $\approx 547$  km; therefore, the average density  $\rho_{\text{avg}}$  varies only slightly, between about 2010 and  $1970 \text{ kg m}^{-3}$ . An outlier is the case with  $\rho_m = 1250 \text{ kg m}^{-3}$ , for which the  $c$ -axis is higher than expected despite an inferred precision of  $\pm 0.1$  km. The calculated rotational period for this particular  $\rho_m$  value is also higher than the fixed 3.91 hr of Haumea. This suggests that for this particular run, the code likely failed to finish converging. The core properties, in contrast to the semiaxis  $c$ , vary greatly depending on what mantle density is assumed. For  $\rho_m = 921 \text{ kg m}^{-3}$ , the core's density must be  $2700 \text{ kg m}^{-3}$ , and it must comprise 84% of Haumea's mass. For

$\rho_m = 1600 \text{ kg m}^{-3}$ , the core's density is  $3500 \text{ kg m}^{-3}$ , and the core must comprise only 44% of Haumea's mass. To within the spatial resolution of the grid (about  $\pm 3$  km), both the outer and the core–mantle boundary conform to triaxial ellipsoids with the given semiaxes.

Also listed in Table 1 are the fraction of Haumea's mass that must be ice, which varies from 16% to 41% across the range of mantle densities, and the fraction of the mantle volume that must be ice, which varies from 100% under the assumption that the mantle is pure ice to 73% at the highest assumed mantle density. The total angular momentum is insensitive to  $\rho_m$ , varying by only a few percent between about  $5.75$  and  $5.51 \times 10^{29} \text{ kg m}^2 \text{ s}^{-1}$  across the range of  $\rho_m$  we considered. It is not obvious what the mantle density must be, but spectroscopic observations suggest that Haumea's surface must be  $>90\%$  water ice, which would argue for  $\rho_m < 1100 \text{ kg m}^{-3}$  and  $J \geq 5.54 \times 10^{29} \text{ kg m}^2 \text{ s}^{-1}$ . As discussed in Section 5.1, we actually favor a slightly lower value for Haumea's present-day angular momentum and define  $J_H \equiv 5.49 \times 10^{29} \text{ kg m}^2 \text{ s}^{-1}$ . This would be consistent with a pure ice mantle but partially dehydrated core.

### 3.2. Immediate Postimpact Haumea

In our proposed scenario, the evolution of Haumea began when two equally large ( $R \approx 640$  km), partially differentiated bodies collided. As the simulations of Desch et al. (2009) and Neveu et al. (2015a) demonstrate, KBOs in this size range differentiate from the inside out, forming a rocky core and icy mantle overlaid by an undifferentiated rock–ice crust. We favor a rock–ice mass ratio of 0.72:0.28 (Section 5.1), so if differentiation is only, say, 20% complete at the time of the impact, each impactor might have a rocky core containing 15% of the total mass and an ice mantle containing 5% of the mass, with the outermost 80% of the mass being undifferentiated rock and ice. We assume the rocky core is composed solely of anhydrous silicates, such as those that dominate the Stardust cometary sample return (Brownlee et al. 2006). The icy component may or may not contain carbon-rich phases like those inferred by the Rosetta mission to exist in comet 67P (Fulle et al. 2017), but any ice that melts will likely separate into pure water ice and other phases (e.g., Neveu et al. 2015b). We hypothesize that these similarly sized bodies collided slowly and obliquely in a graze-and-merge impact, the type of impact that maximizes the angular momentum of the final object (Leinhardt et al. 2010). We favor an impact similar to simulation 4 of Leinhardt et al. (2010), in which two identical bodies with radii of 650 km and bulk densities of  $1960 \text{ kg m}^{-3}$  collided at  $0.9 \text{ km s}^{-1}$  with an impact parameter  $b = 0.6$ . About 6% of the initial mass was lost from the system, and another 1% remained in orbit around the new Haumea.

Adopting similar parameters, we assume the two impactors must add up to a mass of  $1.07 \times 1.03 M_H$ , consistent with two equal bodies with bulk densities of  $1960 \text{ kg m}^{-3}$  and radii of 645 km. Ignoring the angular momentum carried off by the escaping particles, the angular momentum must exceed  $1.14 J_H$ , or  $6.25 \times 10^{29} \text{ kg m}^2 \text{ s}^{-1}$ . Using Equation (1) of Canup (2005), we calculate  $J' = 2.16 \times 10^{30} \text{ kg m}^2 \text{ s}^{-1}$ , and the normalized impact parameter  $b'$  times the impact velocity  $V_{\text{imp}}$  must satisfy

$$b' \left( \frac{V_{\text{imp}}}{0.9 \text{ km s}^{-1}} \right) > 0.49. \quad (4)$$

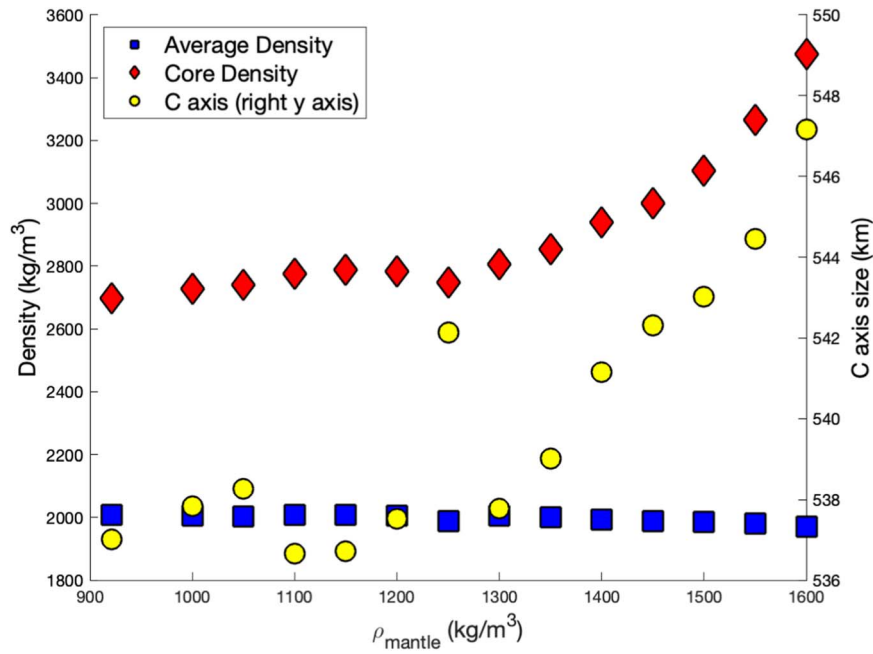


**Figure 2.** Variation with assumed mantle density  $\rho_m$  of calculated semiaxis  $c$ , average density  $\rho_{\text{avg}}$ , and core density  $\rho_c$  for the case of modern-day Haumea.

**Table 1**  
Self-consistent Solutions for Present-day Haumea, Assuming Different Mantle Densities

| $\rho_m$<br>( $\text{kg m}^{-3}$ ) | $P$<br>(hr) | $a$<br>(km) | $b$<br>(km) | $c$<br>(km) | $\bar{\rho}$<br>( $\text{kg m}^{-3}$ ) | $a_c$<br>(km) | $b_c$<br>(km) | $c_c$<br>(km) | $\rho_c$<br>( $\text{kg m}^{-3}$ ) | $M_c$<br>( $10^{21}$ kg) | Total Ice<br>Mass (%) | Mantle Ice<br>Volume (%) | $J$<br>( $10^{29}$ $\text{kg m}^2 \text{s}^{-1}$ ) |
|------------------------------------|-------------|-------------|-------------|-------------|--|---------------|---------------|---------------|------------------------------------|--------------------------|-----------------------|--------------------------|--|
| 921                                | 3.90        | 1056        | 840         | 537.0       | 2008                                   | 882.0         | 720.0         | 468.0         | 2697                               | 3.36                     | 16.2                  | 100.0                    | 5.75   |
| 1000                               | 3.90        | 1056        | 840         | 537.8       | 2005                                   | 864.0         | 708.0         | 462.0         | 2729                               | 3.23                     | 18.5                  | 95.6                     | 5.61   |
| 1050                               | 3.90        | 1056        | 840         | 538.3       | 2003                                   | 852.0         | 702.0         | 462.0         | 2740                               | 3.17                     | 19.4                  | 92.9                     | 5.56   |
| 1100                               | 3.89        | 1056        | 840         | 536.7       | 2009                                   | 846.0         | 696.0         | 456.0         | 2775                               | 3.12                     | 20.0                  | 90.3                     | 5.54   |
| 1150                               | 3.89        | 1056        | 840         | 536.7       | 2009                                   | 834.0         | 690.0         | 450.0         | 2787                               | 3.02                     | 21.5                  | 87.7                     | 5.51   |
| 1200                               | 3.90        | 1056        | 840         | 537.4       | 2006                                   | 828.0         | 684.0         | 450.0         | 2783                               | 2.97                     | 22.0                  | 85.0                     | 5.52   |
| 1250                               | 3.95        | 1056        | 840         | 542.1       | 1989                                   | 822.0         | 672.0         | 450.0         | 2748                               | 2.86                     | 23.4                  | 82.0                     | 5.53   |
| 1300                               | 3.91        | 1056        | 840         | 537.8       | 2005                                   | 804.0         | 666.0         | 438.0         | 2806                               | 2.76                     | 24.9                  | 79.9                     | 5.56   |
| 1350                               | 3.92        | 1056        | 840         | 539.0       | 2000                                   | 786.0         | 648.0         | 432.0         | 2854                               | 2.63                     | 26.7                  | 77.8                     | 5.59   |
| 1400                               | 3.92        | 1056        | 840         | 541.2       | 1992                                   | 756.0         | 630.0         | 420.0         | 2940                               | 2.46                     | 29.4                  | 76.2                     | 5.61   |
| 1450                               | 3.92        | 1056        | 840         | 542.3       | 1988                                   | 732.0         | 612.0         | 414.0         | 3000                               | 2.33                     | 31.2                  | 74.5                     | 5.67   |
| 1500                               | 3.92        | 1056        | 840         | 543.0       | 1986                                   | 696.0         | 588.0         | 402.0         | 3104                               | 2.14                     | 34.2                  | 73.5                     | 5.72   |
| 1550                               | 3.92        | 1056        | 840         | 544.5       | 1981                                   | 654.0         | 558.0         | 384.0         | 3267                               | 1.92                     | 38.2                  | 73.2                     | 5.76   |
| 1600                               | 3.91        | 1056        | 840         | 547.2       | 1970                                   | 612.0         | 528.0         | 372.0         | 3475                               | 1.75                     | 41.4                  | 73.4                     | 5.84   |

Even including the angular momentum of the escaping particles, very reasonable combinations of impact parameter and impact speed would yield a configuration with our hypothesized mass and angular momentum.

An essential aspect of a giant impact is its ability to sort the impacting materials by density. In the simulations of Leinhardt et al. (2010), ice neither melts nor vaporizes but is warmed and severely deformed and fragmented. As they stated, the ice behaves as a slurry with negligible cohesion and low friction. We conclude that not only will the rocky cores of the partially differentiated impactors merge and settle to the center, but the ice will end up on Haumea's surface following the impact. A mass of ice equaling 5% of the original mass ( $0.055 M_H$ ) would yield an ice layer on Haumea about 31 km thick.

The dimensions and other properties of the postimpact configuration are not essential, so we approximate them using the example of a uniform-density body. If the postimpact body is considered to have uniform density, then it would conform to

a Jacobi ellipsoid, for which relationships between the axis ratios, spin rate, and density are known. We can therefore identify Jacobi ellipsoid solutions that match the pre-fling mass and angular momentum of Haumea. For the reasons explained below, we fix these at  $M = 1.03 M_H$  and  $J \approx 1.14 J_H$  and a uniform density of  $1960 \text{ kg m}^{-3}$ . With a mean radius  $r = (abc)^{1/3} = 795 \text{ km}$ , the normalized angular momentum  $\hat{J} = J/(GM^3r)^{1/2} = 0.324$ . From the theory of Jacobi ellipsoids (Chandrasekhar 1969), the axis ratios conforming to this value of  $\hat{J}$  are  $b/a = 0.724$  and  $c/a = 0.454$ , which yield  $a = 1152$ ,  $b = 835$ , and  $c = 523 \text{ km}$ . The consistency between the mass, angular momentum, and other properties actually demands the average density  $\rho_{\text{avg}} = 1960 \text{ kg m}^{-3}$ . The angular velocity can then be determined in two ways. One is to calculate the MOI  $I = M(a^2 + b^2)/5 = 1.67 \times 10^{33} \text{ kg m}^2 \text{ s}^{-1}$  and combine it with the angular momentum  $J = 6.25 \times 10^{29} \text{ kg m}^2 \text{ s}^{-1}$  to derive  $\omega = 3.74 \times 10^{-4} \text{ s}^{-1}$ , corresponding to a spin period  $P = 2\pi I/J = 4.67 \text{ hr}$ . The other way is to note

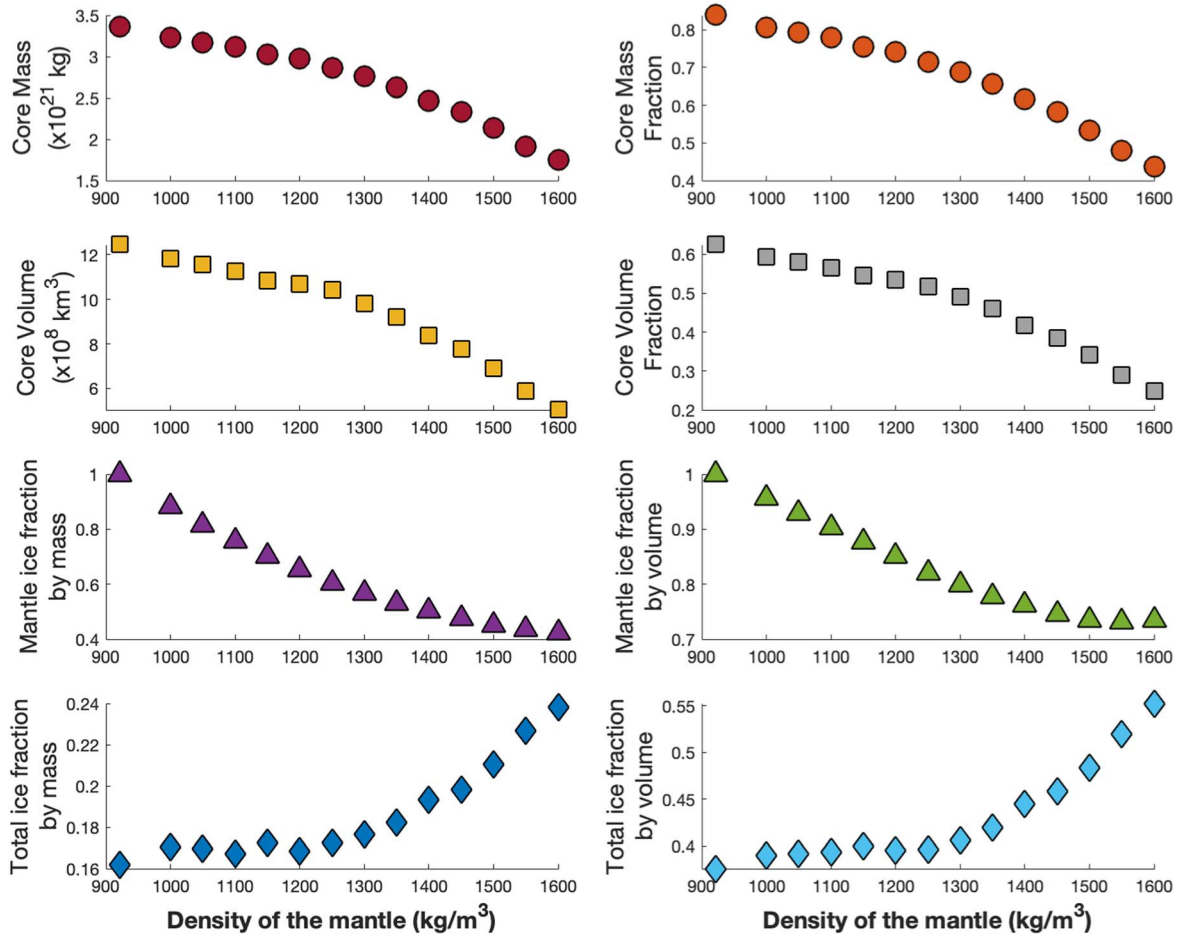


**Figure 3.** Variation with assumed mantle density  $\rho_m$  of various outputs calculated using the *kyushu* code. Generally, the increase in mantle density corresponds to an increase in core density  $\rho_c$  and a decrease in the core size, as well as an increase in the overall ice fraction.

that the parameter  $\omega^2/(2\pi G\rho_{\text{avg}})$  correlates one-to-one with  $\hat{J}$  and for the value above must be 0.416 (Chandrasekhar 1969), yielding  $\omega = 3.77 \times 10^{-4} \text{ s}^{-1}$ . This demonstrates consistency among the assumed parameters.

Although the impactors were partially differentiated, and Haumea was born with a small rocky core and thin ice crust, we approximate its state as a uniform-density body with density  $\rho_{\text{avg}} \approx 1960 \text{ kg m}^{-3}$  to derive its initial rotation period, 4.67 hr. Compared to modern-day Haumea, this configuration would have  $\approx 14\%$  higher angular momentum and deviate more strongly from a sphere. Over time, we assume that radiogenic heating within the postimpact Haumea would lead to differentiation of Haumea and formation of a large rocky core.

### 3.3. Pre-fling Haumea

As will become apparent below, we seek solutions for the pre-fling Haumea, before material is flung from it, that have mass  $M = 1.03 M_{\text{H}}$  and angular momentum  $J \approx 1.14 J_{\text{H}}$ . They also must have a sufficient spin rate that the gravitational acceleration  $g$  along the tip of the  $a$ -axis is completely counteracted by the centrifugal acceleration there,  $\omega^2 a$ , where  $\omega = (2\pi/P)$ . That is, we seek solutions for which  $g_{\text{eff}} = g - \omega^2 a < 0$ . In that case, material from the surface of Haumea—essentially pure water ice—can go directly into orbit around Haumea and, presumably, eventually escape it altogether. As we expect the rotation period to be shorter than the modern-day value of 3.92 hr, we do not put lower limits on the period. We

used the *kyushu* code to run 30 simulations across parameter space and searched the parameter space for solutions that yield  $M = 1.03 M_{\text{H}}$ ,  $J > 1.1 J_{\text{H}}$ , and  $g_{\text{eff}} < 0$ .

Out of these 30 simulations, we found two (cases 18 and 41) that met all criteria and one (case 16) with slightly lower  $J$ , as listed in Table 2. For case 18,  $a = 1128 \text{ km}$ ,  $b = 840 \text{ km}$ ,  $P = 3.42 \text{ hr}$ , and  $J = 1.15 J_{\text{H}}$ . For case 41,  $a = 1128 \text{ km}$ ,  $b = 840 \text{ km}$ ,  $P = 3.48 \text{ hr}$ , and  $J = 1.14 J_{\text{H}}$ . For case 16,  $a = 1104 \text{ km}$ ,  $b = 840 \text{ km}$ ,  $P = 3.39 \text{ hr}$ , and  $J = 1.11 J_{\text{H}}$ .

Compared to modern-day Haumea, the pre-fling cases have smaller cores with significantly higher core densities,  $\rho_c \approx 3700 \text{ kg m}^{-3}$ , consistent with anhydrous silicates. The pre-fling cases all involve a faster (about 13%) spin rates but no periods shorter than 3.4 hr. The pre-fling cases have longer  $a$ -axes but comparable  $b$ - and  $c$ -axes, consistent with the idea that mass will be lost from the end of the long axis. After the loss of material from the tip of the  $a$ -axis, water ice would possibly flow along the surface to the long axis to restore hydrostatic equilibrium. In all cases, the rotational velocity at the tip of the long axis is  $\approx 0.6 \text{ km s}^{-1}$ , suggesting that this is a typical speed at which material would leave Haumea.

The parameters of case 18 are as follows. Compared to modern-day Haumea, this pre-fling Haumea spun faster ( $P = 3.417 \text{ hr}$ ) and was more elongated ( $b/a = 0.74$ ). The core density was  $3860 \text{ kg m}^{-3}$ , and the core semi-axes were  $732 \times 642 \times 432 \text{ km}$ , giving it a mass of  $3.28 \times 10^{21} \text{ kg}$ , about 80.0% of the body's mass. The pressure at the core-mantle

**Table 2**  
Self-consistent Solutions for a Pre-fling Haumea with Mass  $M = 1.03 M_H$

| Case No. | $\rho_m$<br>( $\text{kg m}^{-3}$ ) | $P$<br>(hr) | $a$<br>(km) | $b$<br>(km) | $c$<br>(km) | $\bar{\rho}$<br>( $\text{kg m}^{-3}$ ) | $a_c$<br>(km) | $b_c$<br>(km) | $c_c$<br>(km) | $\rho_c$<br>( $\text{kg m}^{-3}$ ) | $M_c$<br>( $10^{21}$ kg) | $g_{\text{eff}}$<br>( $\text{m s}^{-2}$ ) | $J$<br>( $10^{29}$ $\text{kg m}^2 \text{s}^{-1}$ ) |
|----------|------------------------------------|-------------|-------------|-------------|-------------|--|---------------|---------------|---------------|------------------------------------|--------------------------|---|--|
| 16       | 921                                | 3.393       | 1104        | 840         | 528.3       | 2011                                   | 714           | 636           | 426           | 3976                               | 3.22                     | -0.0276                                   | 6.07   |
| 18       | 921                                | 3.417       | 1128        | 840         | 526.8       | 1973                                   | 732           | 642           | 432           | 3858                               | 3.28                     | -0.0371                                   | 6.31   |
| 41       | 921                                | 3.475       | 1128        | 840         | 530.4       | 1960                                   | 744           | 648           | 426           | 3724                               | 3.25                     | -0.0143                                   | 6.24   |

**Note.** Estimated uncertainties in output quantities:  $\pm 3.3$  km ( $c$  semiaxis),  $\pm 12$   $\text{kg m}^{-3}$  (average density),  $\pm 22$   $\text{kg m}^{-3}$  (core density), and  $\pm 0.031$  hr (period).

**Table 3**  
Self-consistent Solutions for a Post-fling Haumea with Mass  $M = 1.00 M_H$  and a Dense Core

| Case No. | $\rho_m$<br>( $\text{kg m}^{-3}$ ) | $P$<br>(hr) | $a$<br>(km) | $b$<br>(km) | $c$<br>(km) | $\bar{\rho}$<br>( $\text{kg m}^{-3}$ ) | $a_c$<br>(km) | $b_c$<br>(km) | $c_c$<br>(km) | $\rho_c$<br>( $\text{kg m}^{-3}$ ) | $M_c$<br>( $10^{21}$ kg) | $g_{\text{eff}}$<br>( $\text{m s}^{-2}$ ) | $J$<br>( $10^{29}$ $\text{kg m}^2 \text{s}^{-1}$ ) |
|----------|------------------------------------|-------------|-------------|-------------|-------------|--|---------------|---------------|---------------|------------------------------------|--------------------------|---|--|
| 42       | 921                                | 3.454       | 1080        | 840         | 529.4       | 1991                                   | 708           | 636           | 426           | 3875                               | 3.11                     | +0.003                                    | 5.69   |
| 43       | 921                                | 3.485       | 1080        | 840         | 527.3       | 1999                                   | 732           | 642           | 432           | 3708                               | 3.15                     | +0.021                                    | 5.69   |
| 45       | 921                                | 3.400       | 1104        | 840         | 529.4       | 1948                                   | 684           | 624           | 420           | 4103                               | 3.08                     | -0.047                                    | 5.83   |
| 46       | 921                                | 3.492       | 1104        | 840         | 529.5       | 1947                                   | 726           | 636           | 426           | 3737                               | 3.08                     | +0.000                                    | 5.78   |
| 51       | 921                                | 3.489       | 1128        | 840         | 528.5       | 1910                                   | 726           | 642           | 426           | 3718                               | 3.09                     | -0.028                                    | 6.00   |
| 55       | 921                                | 3.502       | 1056        | 840         | 526.1       | 2049                                   | 744           | 648           | 432           | 3625                               | 3.16                     | +0.057                                    | 5.56   |

boundary was  $P_{\text{CMB}} = 54$  MPa. Runs 16 and 41, the only other models we found that had  $g_{\text{eff}} < 0$ , yielded similar results for the core. Case 41 had a core with density  $3720$   $\text{kg m}^{-3}$  and mass  $3.25 \times 10^{21}$  kg with  $P_{\text{CMB}} = 53$  MPa. Case 16 had a core with density  $3980$   $\text{kg m}^{-3}$  and mass  $3.25 \times 10^{21}$  kg with  $P_{\text{CMB}} = 56$  MPa.

For any of these cases, material sitting on the tip of the long axis will effectively experience zero effective gravity. In the context of the work by Scheeres (1994) on gravitational potentials around triaxial ellipsoids, the gravitational potential around Haumea can generally be expected to be a type II ellipsoid. In the cases where  $g_{\text{eff}} \approx 0$  on the long axis, the long axis can be assumed to extend all the way to the unstable saddle points that join trajectories near Haumea with trajectories escaping Haumea. Material orbiting Haumea on a circular orbit with frequency  $\omega$  will steadily move away from the saddle point and go into an unstable direct orbit around Haumea itself, either crashing back onto Haumea or escaping from it.

Material that escapes from Haumea carries away angular momentum. Material ejected from the long axis of the pre-fling Haumea has specific angular momentum  $a^2 (2\pi/P)$ . For runs 16, 18, and 41, these values are 6.27, 6.50, and  $6.39 \times 10^8$   $\text{m}^2 \text{s}^{-1}$ . Loss of mass  $\delta M$  from the long axis will therefore carry away angular momentum  $(\delta J) = 4.6(\delta M/M_H) J_H$ , and a loss of 3% of Haumea's mass during the flinging process should carry away up to  $\approx 14\%$  of present-day Haumea's angular momentum. This represents a maximum loss of angular momentum, as impacts may liberate and provide escape velocity to material closer to the rotation axis. We consider it reasonable to assume that loss of mass  $\delta M$  flung off from near the tip of Haumea's long axis would carry away an average angular momentum  $(\delta J) \approx 4.6(\delta M/M_H) J_H$ . As flinging of material decreased Haumea's mass from  $M = 1.03$  to  $1.00 M_H$ , the angular momentum would have decreased from about  $J = 1.14 J_H = 6.24 \times 10^{29}$   $\text{kg m}^2 \text{s}^{-1}$  to something close to our adopted modern-day value,  $J \approx J_H = 5.49 \times 10^{29}$   $\text{kg m}^2 \text{s}^{-1}$ . The high angular momentum of the pre-fling state is therefore most consistent with cases 18 and 41, and we include case 16 for comparison. We include the outputs of all simulations and a graphical representation of their total angular momentum  $J_H$  in the [Appendix](#).

### 3.4. Post-fling Haumea

Following the flinging of material from near the long axis of the pre-fling Haumea state, we assume that the mass of the new post-fling state is the modern-day value  $M = 1.00 M_H$ , and its new angular momentum is close to the modern-day value  $J \approx J_H = 5.49 \times 10^{29}$   $\text{kg m}^2 \text{s}^{-1}$ . We do not assume that its core resembles the core of modern-day Haumea, which may have resulted from the serpentinization over time of a denser, rockier core. Instead, we seek solutions whose cores match the core properties (mass  $M_c$ , density  $\rho_c$ , core-mantle boundary pressure  $P_{\text{CMB}}$ ) of case 18 above (or 41 or 16), which are consistent with anhydrous silicates. Because these cases necessarily have denser cores and smaller MOIs than modern-day Haumea, their spin rates are likely much faster than modern-day Haumea. We put no lower limits on the period. We search the parameter space for solutions that meet these criteria.

We found several cases that match modern-day Haumea's mass and angular momentum with a denser core, listed in Table 3. We particularly favor cases 43 and 55, as they correspond to the highest core masses ( $M_c = 3.15$  and  $3.16 \times 10^{21}$  kg), closest to the masses of cases 18 and 41 ( $3.28$  and  $3.25 \times 10^{21}$  kg). Based on the convergence tests we ran, we estimate the uncertainty in core densities to be  $\pm 70$   $\text{kg m}^{-3}$  (about 2%), the uncertainties in the axes to each be  $\pm 3$  km (about 0.4%), and the uncertainties in the core mass to be about 3%. The density of the cores of cases 43 and 55 ( $\rho_c = 3708$  and  $3625 \times 10^{21}$   $\text{kg m}^{-3}$ ) also match the core densities of cases 18 and 41 ( $3858$  and  $3724 \times 10^{21}$   $\text{kg m}^{-3}$ ). The core-mantle boundary pressures of cases 43 and 55 ( $P_{\text{CMB}} = 53$  and  $51$  MPa) also provide an excellent match to those of cases 18 and 41 ( $54$  and  $53$  MPa). We particularly favor the match between cases 41 and 55. The core volumes match to within  $< 0.1\%$ , and the core masses and densities and core-mantle boundary pressures match to within 4%.

The match between these cases is also depicted graphically in Figure 4, which also makes clear that the best match in core volume is between case 41 for the pre-fling Haumea and case 55 for the post-fling Haumea. For case 55,  $a = 1056$  km,  $b = 840$  km,  $P = 3.50$  hr, and  $J = 1.01 J_H$ .



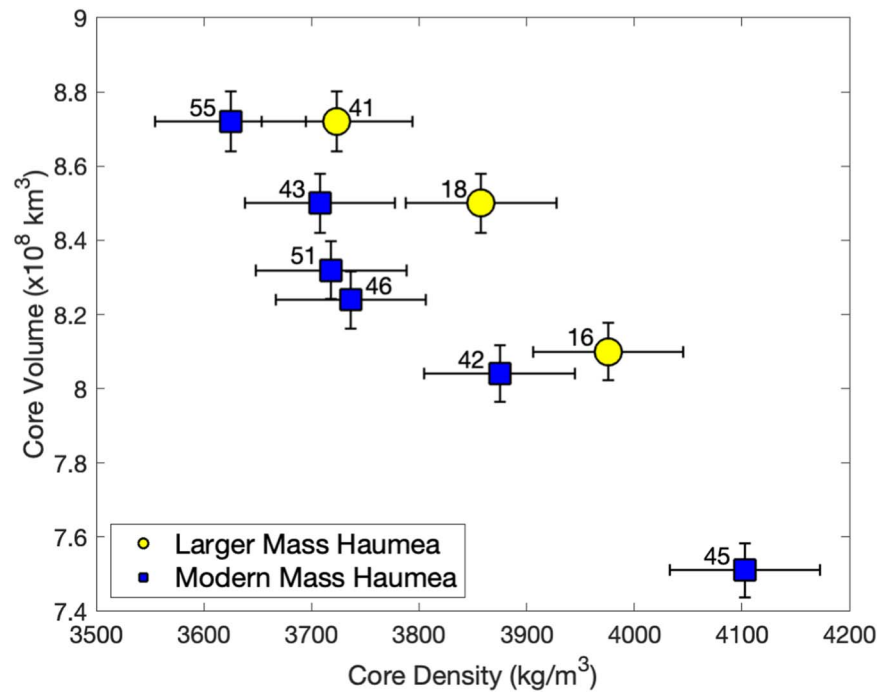


**Figure 4.** Calculated volume and density of cores for pre- and post-fling solutions (labeled with run number), demonstrating that both the high-mass, high angular momentum pre-fling states and the modern-mass, modern angular momentum post-fling cases can share common core properties. We particularly favor case 41 for the pre-fling state and case 55 for the post-fling state.

**Table 4**  
Proposed Evolutionary States of Haumea

| State                       | $M$<br>( $M_H$ ) | $J$<br>( $J_H$ ) | $P$<br>(hr) | $a$<br>(km) | $b$<br>(km) | $c$<br>(km) | $\bar{\rho}$<br>( $\text{kg m}^{-3}$ ) | $\rho_m$<br>( $\text{kg m}^{-3}$ ) | $\rho_c$<br>( $\text{kg m}^{-3}$ ) | $a_c$<br>(km) | $b_c$<br>(km) | $c_c$<br>(km) | $M_c$<br>( $M_H$ ) |
|-----------------------------|------------------|------------------|-------------|-------------|-------------|-------------|--|------------------------------------|------------------------------------|---------------|---------------|---------------|--------------------|
| Postimpact (end of stage 2) | 1.03             | 1.14             | 4.65        | 1152        | 835         | 523         | 1960                                   | ...                                | ...                                | ...           | ...           | ...           | ...                |
| Pre-fling (end of stage 3)  | 1.03             | 1.14             | 3.48        | 1128        | 840         | 530         | 1960                                   | 921                                | 3724                               | 744           | 648           | 426           | 0.81               |
| Post-fling (end of stage 4) | 1.01             | 0.97             | 3.50        | 1056        | 840         | 526         | 2049                                   | 921                                | 3625                               | 744           | 648           | 432           | 0.79               |
| Today (stage 6)             | 1.00             | 1.00             | 3.92        | 1056        | 840         | 537         | 2008                                   | 921                                | 2697                               | 882           | 720           | 468           | 0.84               |

**Note.** Values are relative to those of present-day Haumea. Here  $M_H \equiv 4.006 \times 10^{21}$  kg, and  $J_H \equiv 5.49 \times 10^{29}$   $\text{kg m}^2 \text{s}^{-1}$ .

### 3.5. Summary

Putting these results in chronological order suggests a plausible scenario for the evolution of Haumea, summarized in Table 4.

First, two nearly equal-sized KBOs with radii of  $\approx 640$  km collided and merged in a graze-and-merge type collision (Leinhardt et al. 2010). During the impact, about 6% of the mass was ejected, but these bodies would not form a dynamically coherent family today. The giant impact resulted in a Haumea with mass  $M \approx 1.03 M_H$  and angular momentum  $J \approx 1.14 J_H$ , spinning about once per 4.7 hr. The impactors, we hypothesize, were partially differentiated, leaving a thin crust of water ice on the surface of Haumea. Approximated as a Jacobi ellipsoid with a uniform density of  $\approx 1960 \text{ kg m}^{-3}$ , Haumea would have semiaxes of  $1152 \times 835 \times 523$  km.

Following the impact, radiogenic heating from inside Haumea led to differentiation and formation of a core. The end stages of differentiation would culminate in a pre-fling configuration similar to case 41: mass  $M = 1.03 M_H$  and angular momentum  $J = 1.14 J_H$ ; a rocky core of density  $\rho_c = 3724 \text{ kg m}^{-3}$  and mass  $M_c = 3.25 \times 10^{21}$  kg; an icy mantle with density  $\rho_m = 921 \text{ kg m}^{-3}$ ; and a boundary between them at a depth corresponding to  $P_{\text{CMB}} = 53$  MPa. The average

density of this configuration would be  $\rho_{\text{avg}} = 1960 \text{ kg m}^{-3}$ . Because the MOI decreased so much during core formation, the spin period decreased from 4.7 to only 3.5 hr. This led to more extreme elongation of the triaxial ellipsoid and semiaxes of  $1128 \times 840 \times 530$  km. The configuration remained in hydrostatic equilibrium, but the increased spin rate led to such high centrifugal forces at the tip of the  $a$ -axis that the effective gravity vanished,  $g_{\text{eff}} < 0$ . Any material near the tip of the long axis could have been lifted off of Haumea, passed through the saddle point of the potential into orbit around Haumea, and eventually launched into space.

Removal of about 3% of the body's mass also would have removed angular momentum, leaving the body in a post-fling state like case 55: mass  $M = 1.00 M_H$  and angular momentum  $J = 1.01 J_H$ ; a rocky core of density  $\rho_c = 3625 \text{ kg m}^{-3}$  and mass  $M_c = 3.16 \times 10^{21}$  kg; an icy mantle with density  $\rho_m = 921 \text{ kg m}^{-3}$ ; and a boundary between them at a depth corresponding to  $P_{\text{CMB}} = 51$  MPa. The average density of this configuration would be  $\rho_{\text{avg}} = 2049 \text{ kg m}^{-3}$ . The loss of angular momentum and mass from the long axis led (after relaxation of Haumea) to a less extreme elongation and semiaxes of  $1080 \times 840 \times 526$  km. In this new configuration,  $g_{\text{eff}} > 0$ , and further mass loss was inhibited.

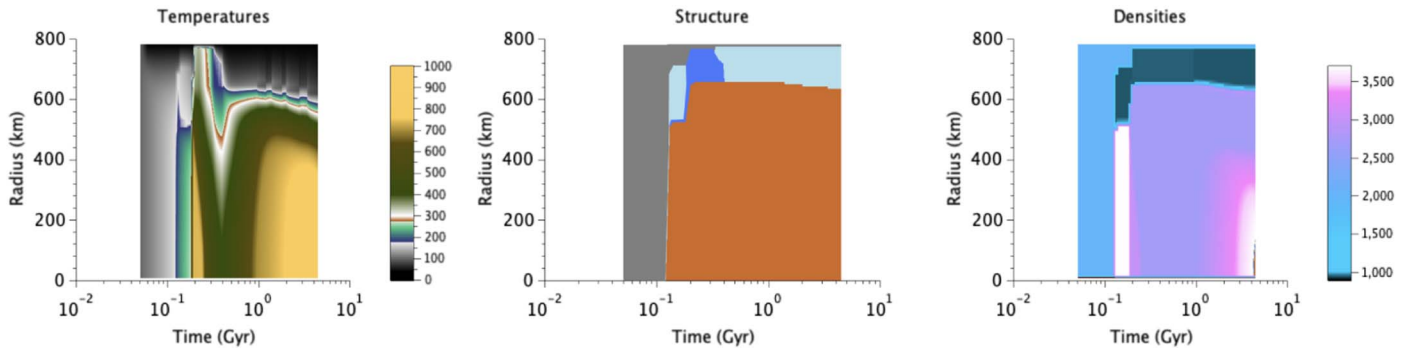


**Figure 5.** Thermal and geophysical evolution of a spherical object with a mass and bulk density close to Haumea’s. Temperature (left; in K), interior structure (middle; gray = undifferentiated, sky blue = ice, dark blue = liquid water, brown = rock), and density (right; in  $\text{kg m}^{-3}$ ) are shown as a function of radius and time. Differentiation and hydration take place largely sequentially in the first 100 Myr postimpact.

Finally, further radiogenic heating inside Haumea melted ice and allowed water to circulate through the core, allowing serpentinization of this material. This enlarged the core and lowered its density. Today, Haumea is consistent with an effectively pure water-ice mantle and core with density  $\rho_c \approx 2700 \text{ kg m}^{-3}$ , a typical density for hydrated silicates (Dunham et al. 2019). The semiaxes of Haumea today are consistent with  $1056 \times 840 \times 537 \text{ km}$  and an average density of  $2008 \text{ kg m}^{-3}$ .

It is very significant that the average and core densities maintain continuity across key stages. The uniform-density postimpact state is consistent with having the same overall density ( $\rho_{\text{avg}} = 1960 \text{ kg m}^{-3}$ ) as the immediate pre-fling state, implying continuity of its composition. Likewise, the average density of the post-fling state,  $\rho_{\text{avg}} = 2049 \text{ kg m}^{-3}$ , differs by only 2.0% from the density we infer for modern-day Haumea, reflecting the similarity of composition during these stages. During the flinging process, the loss of  $0.03 M_{\text{H}}$  of pure water ice should have increased the average density by about 3.5%, or about  $70 \text{ kg m}^{-3}$ . We find that the preferred density of modern-day Haumea is about 2.4% higher than the pre-fling state, equaling the expected change to within the uncertainties of the calculation. Likewise, the core properties of the pre- and post-fling Haumea configurations match to within  $<3\%$ , less than the inherent uncertainties in the problem, consistent with the expected continuity of core properties as icy material is flung from the surface.

#### 4. Internal Evolution of Haumea

To verify whether the sequence of differentiation and core hydration is consistent with the processes driving Haumea’s internal evolution (radiogenic heating, conductive and convective cooling) and to estimate the timing of these events, we simulate the thermal and geophysical evolution of a spherical object of bulk density  $2008 \text{ kg m}^{-3}$  and  $R = 781 \text{ km}$  radius (i.e., mass =  $M_{\text{H}}$ ) using the previously developed one-dimensional code *IcyDwarf* of Neveu et al. (2015a; <https://github.com/MarcNeveu/IcyDwarf>). This numerical model enables explicit simulation of ice–rock differentiation by melting and gravitational instability and of rock (de)hydration. One caveat of *IcyDwarf* is that, because it is a one-dimensional code, it mandates that the body being studied is spherical, which Haumea is decidedly not. We discuss potential implications for this later in this section and in Section 5.

Here *IcyDwarf* is set up as described in Neveu et al. (2015a), except for an upgraded treatment of hydrothermal heat

transfer. Rather than using Equation (27) of Neveu et al. (2015a) to set an effective thermal conductivity  $k_{\text{hydro}}$  in porous (cracked) core grid zones experiencing hydrothermal circulation (i.e., if the Rayleigh number  $Ra$  exceeds a critical value  $Ra_{\text{cr}}$ ),  $k_{\text{hydro}}$  is instead calculated by multiplying the rock thermal conductivity of  $1\text{--}4.2 \text{ W m}^{-1} \text{ K}^{-1}$  (Neveu et al. 2015a, and references therein) by the Nusselt number  $Nu = (Ra/Ra_{\text{cr}})^{2/3 + Ra_{\text{cr}}/Ra}$ , with  $Ra_{\text{cr}} = 40$ . This expression is a fit to numerical simulations of hydrothermal convection to investigate the  $Nu$ – $Ra$  relationship for convection in porous media in the range  $Ra = 40\text{--}4000$  (Huang & Wellmann 2021). This revised approach makes the transition between convective and conductive heat transfer smoother, improving code stability in addition to model fidelity. For numerical stability,  $k_{\text{hydro}}$  is still capped at  $100 \text{ W m}^{-1} \text{ K}^{-1}$ , a value reached around  $Ra = 40,000$ .

We assume that the impact takes place at 50 Myr after  $t = 0$ , i.e., formation of calcium-rich, aluminum-rich inclusions (CAIs). We run the simulation from that time until 4500 Myr (present day). The postimpact Haumea is assumed to be free of porosity. The ice melting temperature is depressed due to ammonia, whose abundance relative to water is set to 2 wt%. The rock is assumed to initially be mostly dehydrated, a combination of 90 vol.% of a dry end-member with density  $3820 \text{ kg m}^{-3}$  and 10 vol.% of a hydrated end-member with density  $2700 \text{ kg m}^{-3}$ . The body is assumed to not have been heated significantly by the impact, i.e., to have a uniform initial temperature of 100 K and a 40 K surface. Abundances of radionuclides per  $10^6 \text{ Si}$  atoms (Desch et al. 2009) are assumed to be those of a CV chondrite (Wasson & Kallemeyn 1988):  $2.032 \text{ }^{40}\text{K}$ ,  $0.058 \text{ }^{235}\text{Th}$ ,  $0.008 \text{ }^{235}\text{U}$ , and  $0.025 \text{ }^{238}\text{U}$ . The abundances of these radionuclides in other chondrites differ on a  $\sim 10\%$  level, but this does not significantly affect the timing or extent of differentiation in the body.

Simulation results are shown in Figure 5. Due to radiogenic heating, ice melts in the central regions, triggering differentiation between 70 and 80 Myr after formation. Differentiation is mostly complete by 80 Myr. We neglect rock hydration during that phase, which is appropriate if the settling of rock grains, which takes place by Stokes flow on a timescale  $\tau \sim 9\mu R/[2(\rho_c - \rho_m)gr^2] \sim 10^4 (1 \mu\text{m}/r)^2 \text{ yr}$ , is faster than the timescale of hydration, which is likely to be controlled by migration of a hydration front into the grains on a timescale  $\tau \sim r^2/(2D_{\text{H}_2\text{O}}) \sim 10^{-2} (r/1 \mu\text{m})^2 \text{ yr}$  (Macdonald & Fyfe 1985), with  $D_{\text{H}_2\text{O}} = 4.5 \times 10^{-5} e^{-45000/RT} \text{ m}^2 \text{ s}^{-1}$  (Neveu et al. 2015a) being the diffusion rate of water in rock. This is verified for grains larger than

50  $\mu\text{m}$ . Most of the rocky mass in carbonaceous chondrites (Weisberg et al. 2006) and comet 67P (Fulle et al. 2016) is in millimeter-sized particles.

In this case, a largely dry core forms, but continued radiogenic heating pressurizes any pore water and fractures the core throughout (Neveu et al. 2015a). This creates a setting prone to hydrothermal circulation as soon as sufficient meltwater accumulates above the core–mantle boundary. The onset of hydrothermal circulation and associated core hydration occurs between 130 and 140 Myr after formation. Because hydration is exothermic, the core temperature becomes buffered by its state of hydration; thus, it becomes mostly, but not fully, hydrated. The core density is  $3670 \text{ kg m}^{-3}$  at 130 Myr (postdifferentiation and just before hydration), sharply decreasing to  $2820 \text{ kg m}^{-3}$  by 140 Myr and  $2680 \text{ kg m}^{-3}$  once the core has cooled enough to be completely hydrated (Figure 5). The present-day core density is slightly higher,  $2890 \text{ kg m}^{-3}$ , due to late dehydration of the core as the balance of late radiogenic heating and conductive heat transport in the core and mantle raises the core temperature above 800 K in the central regions. Such late dehydration may not occur in Haumea if its nonspherical shape (i.e., higher surface area–to–volume ratio) and/or nonzero rock content in the icy shell make the internal temperatures lower than those of this simulation.

Finally, an important result from these calculations is that the predicted thickness of the original, undifferentiated rock–ice crust is  $<10 \text{ km}$ . This is in contrast to findings by Desch et al. (2009) that KBOs would retain rock–ice crusts of  $\approx 60 \text{ km}$  in thickness but in keeping with the findings of Neveu et al. (2015a), who found that such thin crusts are common. Thin crusts are attributable to exothermic serpentinization reactions that hydrate the rock and propagate upward in a reaction front. The thinness of Haumea’s rock–ice crust, overlying a convective ice layer, makes it more likely than not to have foundered into the ice layer, allowing Haumea to eventually fully differentiate. This is not modeled by the `IcyD-warf` code.

## 5. Discussion

### 5.1. Haumea’s Composition and Porosity

Our findings reveal a plausible evolutionary history for Haumea but require restricted values for the densities  $\rho_{\text{avg}}$  and  $\rho_c$  over time, with implications for the compositions. The average density following the impact is constrained to be  $\rho_{\text{avg}} \approx 1960 \text{ kg m}^{-3}$ , based on the need to have a uniform-density body with a mass  $M = 1.03 M_{\text{H}}$  and an angular momentum  $J \approx 1.14 J_{\text{H}}$ . Using our favored case for the post-fling state, the average density increased by about 4.5% to  $\bar{\rho} \approx 2049 \text{ kg m}^{-3}$  after Haumea flung off material and ended up with mass  $M = 1.00 M_{\text{H}}$  and  $J = 1.00 J_{\text{H}}$ . This constraint is derived independently but is roughly consistent with the density increase of 3.5% expected after the loss of  $0.03 M_{\text{H}}$  of water ice. The core density after differentiation both before and after the flinging of material is constrained to be  $\rho_c \approx 3700 \text{ kg m}^{-3}$  (assuming the mantle is pure water ice with  $\rho_{\text{m}} = 921 \text{ kg m}^{-3}$ ). This core density is higher than the modern-day value,  $\rho_c \approx 2700 \text{ kg m}^{-3}$ , presumably because of hydration and serpentinization of the rocky core since that time. Remarkably, all of these independently derived constraints

are completely consistent with the compositions expected for each stage of evolution.

First, a density of  $\approx 3700 \text{ kg m}^{-3}$  is high for rocky material, but not unreasonably so. Silicate materials are typically taken to have densities of 3300 (Macke et al. 2011) or 3500 (Bierson & Nimmo 2019)  $\text{kg m}^{-3}$ , and the nonice component is likely to contain metal as well. A likely starting composition for materials in the outer solar system is carbonaceous chondrites. Grain and bulk densities of various carbonaceous chondrites were compiled by Macke et al. (2011), who reported that CV chondrites have grain densities of  $3250\text{--}3680 \text{ kg m}^{-3}$  (averaging  $3540 \text{ kg m}^{-3}$ ) and bulk densities of  $2590\text{--}3460 \text{ kg m}^{-3}$  (averaging  $3030 \text{ kg m}^{-3}$ ), implying porosity in the range 1%–23% (averaging 15%). Likewise, they reported that CR chondrites have grain densities of  $3060\text{--}3880 \text{ kg m}^{-3}$  (averaging  $3420 \text{ kg m}^{-3}$ ) and bulk densities of  $2290\text{--}3940 \text{ kg m}^{-3}$  (averaging  $3110 \text{ kg m}^{-3}$ ), implying porosity in the range 0%–25% (averaging 10%). If the interior of Haumea is similar in composition to either chondrite but with zero porosity, then densities of  $\approx 3700\text{--}3900 \text{ kg m}^{-3}$  would not be unexpected.

Whether Haumea should have zero porosity or a more “typical” porosity of 10% is an open question. It is difficult to assess from first principles; Durham et al. (2005) found that water ice at 77 K could support porosities of 10%–20% even up to 100 MPa, but Yasui & Arakawa (2009) found that water ice at 260 K could not support even 1% porosity at 30 MPa. Bierson & Nimmo (2019) coupled one model for the collapse of porosity with a thermal evolution model for KBOs and found that bodies the size of Haumea typically could retain about 10% porosity, but they noted a number of physical effects not included in their model that could reduce the porosity. Malamud & Prialnik (2015) attempted a semiempirical approach, reviewing the porosities of chondrites and terrestrial sedimentary rocks as a function of their inferred histories. They concluded that for temperatures  $T > 425 \text{ K}$ , peak temperature was the main determinant of whether porosity collapsed, with porosity decreasing linearly with temperature between 425 and 925 K. That is, rocks that ever exceeded 925 K would have zero porosity. These temperatures are easily achieved throughout most of the volumes of KBO cores (Desch et al. 2009), at least until water is able to circulate through the core effectively (Neveu et al. 2015a; this work).

Another effect that could reduce porosity is the shock associated with the impact suffered by Haumea in the first place. As reviewed by Malamud & Prialnik (2015), sedimentary rocks subjected to pressures above about 200 MPa do not maintain any porosity. Within meteorites, peak pressures experienced during shocks can crush porosity and fill pore spaces with melt veins, with collapse tending to be total above peak pressures of 5 GPa (Sharp & de Carli 2006).

Based on the above, a core density  $\rho_c \approx 3700 \text{ kg m}^{-3}$  is exactly in line with the density expected for carbonaceous chondrite rock (especially CR chondrite) that has suffered a complete collapse of porosity, either due to the shock of the impact and/or thermal effects.

Second, the average densities,  $\rho_{\text{avg}} \approx 2000 \text{ kg m}^{-3}$ , we derive are typical for large KBOs and consistent with their inferred rock–ice ratios (Bierson & Nimmo 2019). Our modeling (Table 4) suggests that before hydration of the core, Haumea’s core density was  $\rho_c \approx 3700 \text{ kg m}^{-3}$ , implying a rock

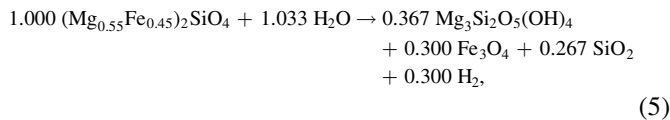
mass fraction of

$$f_{\text{rock}} = \frac{\rho_c}{\rho_{\text{avg}}} \frac{\rho_{\text{avg}} - \rho_{\text{ice}}}{\rho_c - \rho_{\text{ice}}} \approx 0.72.$$

This rock fraction, independently constrained by the need for the pre-/post-fling Haumea states to be rocky cores and icy mantles in hydrostatic equilibrium, is remarkably similar to the mean value of  $f_{\text{rock}} \approx 0.7$  inferred by Bierson & Nimmo (2019) for the vast majority of KBOs by matching the bulk densities of KBOs against a thermal evolution model including porosity. For the specific case of the Haumea with a rock mass fraction  $f_{\text{rock}} = 0.7$ , Bierson & Nimmo (2019) would predict a slightly lower density,  $\approx 1700 \text{ kg m}^{-3}$ , because their modeling suggests that Haumea would retain significant porosity. In contrast, our findings suggest that Haumea did not retain significant porosity after differentiation, achieving a higher bulk density of  $\rho_{\text{avg}} \approx 2000 \text{ kg m}^{-3}$ . Given the success of the Bierson & Nimmo (2019) model for explaining the majority of KBOs, this suggests that Haumea's loss of porosity may be unusual, perhaps associated with the giant impact it suffered.

Finally, it is reasonable to ask whether rock could react with water ice to yield minerals with a density of  $2700 \text{ kg m}^{-3}$ . We infer that Haumea's rock fraction after differentiation had a grain density (and bulk density) of  $\approx 3720 \text{ kg m}^{-3}$ , which appears typical for carbonaceous chondrite materials with no porosity. Following Dunham et al. (2019), we approximate this material as olivine with Mg#55, which is typical for CI chondrites (Macke et al. 2011).

Reaction with water could proceed as



in which 1.00 kg of olivine reacts with 0.110 kg of water to form 0.601 kg of serpentine, 0.411 kg of magnetite, 0.095 kg of silica, and 0.004 kg of hydrogen gas, which escapes the system. Extrapolating between the densities of the end-members forsterite and fayalite, we estimate that the olivine would have a grain density of  $\approx 3740 \text{ kg m}^{-3}$ . In combination with the water, the average grain density of the olivine plus water would be  $2870 \text{ kg m}^{-3}$ . We estimate the average grain density of the serpentine + magnetite + silica assemblage would be  $\approx 3120 \text{ kg m}^{-3}$ . Reaction of water with rock is associated with an increase in porosity. This is observed in the correlation of porosity with oxidation state in carbonaceous chondrites (Macke et al. 2011) and is an expected outcome of chemical reactions (Neveu et al. 2015a). Introduction of 10%–15% porosity, typical in carbonaceous chondrites, would decrease the bulk density of the final mineral assemblage to between 2650 and  $2800 \text{ kg m}^{-3}$ . This is completely consistent with the inferred density of the core of modern-day Haumea,  $\approx 2700 \text{ kg m}^{-3}$ . Consumption of ice during hydration of the core leaves Haumea today with an ice mass fraction of 18%. This simplified way of approaching the geochemistry yields values very close to those of the more sophisticated approach using *IcyDwarf*.

In summary, from the densities we required from structure calculations to maintain hydrostatic equilibrium, we can make

the following inferences. Haumea probably had a rock mass fraction after the giant impact of  $f_{\text{rock}} \approx 0.7$ , exactly in line with the rock mass fractions of other KBOs (Bierson & Nimmo 2019). This alone implies that the collision took place before proto-Haumea mostly differentiated, or else a loss of ice from a stripped mantle may have been expected, increasing  $f_{\text{rock}}$  in Haumea above the values in other KBOs. Haumea probably started with  $0.74 M_{\text{H}}$  of rock and  $0.29 M_{\text{H}}$  of ice, with the excess  $0.03 M_{\text{H}}$  eventually spinning off later. As a result of its thermal history or perhaps due to the shock collapse of porosity due to the giant impact, Haumea had near-zero porosity after differentiation and a core density  $\rho_c \approx 3700 \text{ kg m}^{-3}$ . After flinging off icy material from its surface, Haumea lost 3% of its mass in ice, leaving it with  $0.74 M_{\text{H}}$  of rock and  $0.26 M_{\text{H}}$  of ice. Finally, after cracking occurred in the core and water was able to circulate through the core, hydration of silicates occurred and porosity increased, leading to  $\rho_c \approx 2700 \text{ kg m}^{-3}$ , as inferred for modern-day Haumea. This consumed about  $0.08 M_{\text{H}}$  of ice, leaving Haumea today with a hydrated silicate core of  $0.82 M_{\text{H}}$  and an icy mantle of  $0.18 M_{\text{H}}$ .

## 5.2. Timing of Events in Haumea's Evolution

### 5.2.1. Timing of the Dynamical Instability

Our inferred history of Haumea allows us to place constraints on the timing of key events in solar system history, the first one being the timing of the dynamical instability in the outer solar system. We argue that the giant impact was most likely to occur during the dynamical instability, just as the impactors were beginning to differentiate. Both of these events, we argue, took place after about 70 Myr of solar system evolution.

The evolution of the Kuiper Belt has been divided into three distinct stages (Levison et al. 2008). The first is a quiescent stage conducive to growth, characterized by a Kuiper Belt between 15 and 30 au containing tens of Earth masses and eccentricities and inclinations  $\ll 10^{-2}$ . Classical KBOs are associated with formation in this stage. The second is a dynamical instability associated with Neptune's migration, likely as described by the Nice model instability (Tsiganis et al. 2005). Once this stage is initiated, quantities like the mass of the Kuiper Belt and Neptune's semimajor axis tend to be approached with an e-folding time of around 50 Myr (Malhotra 1993; Tsiganis et al. 2005; Nesvorný & Vokrouhlický 2016). During this stage, Neptune cleared out >99.7% of the Kuiper Belt. Many KBOs, including Haumea, were ejected to the scattered disk; others joined the resonant populations. The third stage is relatively quiet, characterized by a slow loss of members from the scattered disk, depleting it by a factor of  $\sim 10^2$ .

Previous models (e.g., Brown et al. 2007; Leinhardt et al. 2010) that equated the dynamical family with the giant impact have had difficulty simultaneously explaining the likelihood of the giant impact and the existence of the family. Preservation of their dynamical coherence demands that the family members were ejected after Haumea was emplaced in the scattered disk and after the dynamical instability (Levison et al. 2008). However, the probability of a collision between two large (>1000 km diameter) bodies is exceedingly low today and requires the impact to take place before the primordial Kuiper Belt was cleared. As a compromise, Levison et al. (2008) conjectured that at least one of the impactors was an object in a more massive primordial scattered disk, with the collision

happening soon after the dynamical instability; however, the typical impact speeds during this stage are  $\approx 3 \text{ km s}^{-1}$ , which would have led to catastrophic disruption of the impactors (Leinhardt et al. 2010).

By separating the ejection of the Haumeans from the giant impact that imparted such a large angular momentum to Haumea, it is possible to have the giant impact occur at a probable time and the ejection occur after Haumea has joined the scattered disk and after Neptune’s migration, preserving the dynamical coherence of the family. In principle, the high disk masses of either the first or second stages above would be consistent with a high probability of impact, but the inferred impact velocity constrains the impact to occur during the second stage, during the dynamical instability. In the quiescent stage, the typical impact velocities will be  $\sim V_K(e^2 + i^2)^{1/2} < 0.1 \text{ km s}^{-1}$ , where  $V_K \approx 8 \text{ km s}^{-1}$  is the typical Keplerian velocity, and  $e \sim i \ll 10^{-2}$  are the typical eccentricity and inclinations. For an impact velocity of  $\approx 0.9 \text{ km s}^{-1}$  to be expected, the giant impact should occur during the dynamical instability.

Then, as long as the ejection of the Haumeans takes place at least  $\sim 50$  Myr later, it will happen after Haumea has been scattered outward by Neptune and emplaced in the scattered disk. Our thermal modeling suggests that Haumea’s core forms between about 70 and 80 Myr after the impact, so this condition is easily satisfied.

Our model also constrains the timing of the giant impact to be soon after the impactors had started to differentiate. If they had fully differentiated, there would be no delayed spin-up of Haumea or ejection of the Haumeans. If the impactors had not differentiated at all, there would not be pure water ice on the surface of Haumea to eject and form the apparently pure ice family members. Interestingly, McKinnon et al. (2017) concluded (for other reasons) that the Charon-forming giant impact on Pluto also occurred before either body had differentiated much. Thermal evolution models of KBOs of the impactors’ size starting from a “cold start” (initial temperatures of  $\approx 40$  K) show that differentiation initiates about 70–75 Myr after accretion and is completed within 10 Myr (Desch et al. 2009; Desch & Neveu 2015; Neveu et al. 2015a). (It has been argued that Pluto and Charon formed from a “warm start” at a higher initial temperature, Bierson et al. 2020, but these objects formed after a giant impact and were not isolated KBOs.) Accretion of KBOs probably took place  $> 5$  Myr after the formation of CAIs at time  $t = 0$ , so that the KBOs generally did not incorporate live  $^{26}\text{Al}$  (Bierson & Nimmo 2019). Therefore, the impactors probably experienced partial (e.g., 20%) differentiation at around  $t = 77$ –82 Myr. We therefore place the giant impact at about this time; the dynamical instability must have been initiated before this but completed after this time. That is, the initiation of the dynamical instability must have taken place between  $\approx 27$  and 32 Myr at the earliest and shortly before  $t = 77$ –82 Myr at the latest.

Surprisingly, this is consistent with the current understanding of the dynamical instability. Although the initial version of the Nice model was fine-tuned so that it would initiate at 650 Myr after the birth of the solar system, to coincide with the late heavy bombardment (Tsiganis et al. 2005), more recent work suggests that the dynamical instability took place much earlier in the solar system’s evolution. The survival of the Patroclus–Menoetius Trojan binary has been

used to argue that the dynamical instability took place in the first 100 Myr of solar system history (Nesvorný et al. 2018). Recent detailed dynamical simulations by de Sousa et al. (2020) constrain the initiation of the dynamical instability to be roughly 37–62 Myr after solar system formation. DeSousa et al. (2021) recently suggested that the same dynamical instability triggered the Moon-forming impact, which took place at  $60 \pm 10$  Myr after solar system formation according to radiometric dating of lunar samples (Barboni et al. 2017). The instability and Neptune’s migration would have effectively ended about 50 Myr later, around  $t = 87$ –112 Myr. This allows for Haumea to be emplaced in the scattered disk sometime between about  $t = 77$ –82 and 87–112 Myr.

### 5.2.2. Ejection of the Haumeans

The next event in the history of Haumea was the ejection of material from the long axis as the MOI reached its minimum after final differentiation of a rocky core but before significant hydration of the core. In our thermal evolution simulations, core formation starts at 70 Myr and is complete by 80 Myr, after Haumea’s formation after the giant impact. Sometime in that time window is when the MOI of Haumea decreased to its minimum value, allowing ejection of the Haumeans. We therefore infer that the creation of the family took place 70–80 Myr after the giant impact, which we assume took place at about  $t = 77$ –82 Myr. That is, the ejection of the Haumeans took place at  $t = 147$ –162 Myr, or  $4.41 \pm 0.01$  Gyr ago. Because we infer that Haumea was emplaced in the scattered disk by about  $t = 87$ –112 Myr, the ejection of the Haumeans occurred tens of megayears after that. This timing is consistent with the dispersion of the family members’ orbital elements, which requires that the family was generated  $> 1$  Gyr ago (Ragozzine & Brown 2007; Volk & Malhotra 2012) but after Haumea was emplaced by interaction with Neptune in the scattered disk.

### 5.2.3. Hydration of Haumea’s Core

After the ejection of the Haumeans, the next stage in Haumea’s evolution would have been the hydration of its initially anhydrous silicate core. The results of our thermal evolution study (Section 4) suggest that this stage would have followed closely after the ejection at  $\approx 70$ –80 Myr after formation, with the core hydrating almost completely between 130 and 140 Myr after formation. Between about 130 and 380 Myr after formation in our model, i.e., from about  $t = 210$  to 460 Myr, a substantial subsurface liquid ocean existed. This ocean would have comprised about 15% of Haumea’s mass, or about half the mass of Earth’s present-day oceans. Unlike Earth’s oceans, we assume it would have been ammonia-rich, although much less so (3 wt% in the *IcyDwarf* simulation) than the eutectic composition. Its temperature in the simulation briefly peaks at about 350 K (Figure 5). The freezing of this ocean would have inhibited the cooling of the core by hydrothermal circulation of water, leading to an increase in the core temperature peaking after about 2 Gyr of evolution. By the present day, the innermost  $\approx 320$  km of the core (about 12% of the core’s volume) potentially could have dehydrated, although it is also possible that the nonspherical shape of Haumea allowed more effective cooling than we assumed, leading to less dehydration of the core. In any event, Haumea’s core would be largely hydrated at the present time.

**Table 5**  
Proposed Timeline for the Evolution of Haumea

| Universal Time                 | Event  |
|--------------------------------|--|
| $t = 0$                        | Formation of CAIs (about 4568 Myr ago)   |
| $t > 5$ Myr                    | Accretion of most KBOs (Bierson & Nimmo 2019)                                      |
| $t = 37\text{--}62$ Myr        | Initiation of dynamical instability and Neptune's migration (de Sousa et al. 2020) |
| $t \approx 50\text{--}70$ Myr  | Moon-forming impact in inner solar system (Barboni et al. 2017)                    |
| $t = 75\text{--}80$ Myr        | Start of differentiation of Haumea's impactors                                     |
| $t = 77\text{--}82$ Myr        | Giant impact that formed Haumea  |
| $t \approx 87\text{--}112$ Myr | Effective end of dynamical instability (e-folding time 50 Myr)                     |
| $t \approx 80\text{--}110$ Myr | Ejection of Haumea to the scattered disk   |
| $t = 147\text{--}162$ Myr      | Ejection of the Haumean family members   |
| $t \approx 210$ Myr            | Formation of Haumea's subsurface ocean and initial hydration of Haumea's core      |
| $t \approx 460$ Myr            | Freezing of Haumea's subsurface ocean  |
| $t > 1300$ Myr                 | Partial dehydration of Haumea's core   |

**Note.** A timeline of the major events affecting Haumea's formation and evolution.

Haumea would have experienced very little evolution after this partial dehydration event at  $\approx 2$  Gyr and been much the same as today for the past 2.5 Gyr.

### 5.3. Dynamical Distribution of Ejected Family Members

Another constraint that must be met is whether the dynamical distribution of ejected family members in our model matches the observed dynamical distribution of family members and their orbital elements. The ejection of material from the long ( $a$ ) axis of Haumea would be equivalent to planar ejection, a scenario ruled out by Proudfoot & Ragozzine (2019), except for the important distinction that the geophysically driven ejection of the Haumeans would have occurred over a time span of  $\sim 10^7$  yr, not in 1 day. In that case, the dynamical distribution of ejected family members in our proposed model is similar to the much more favorable "delayed ejection planar isotropic" (DEPI) model discussed in Proudfoot & Ragozzine (2019; see their Figure 4 for more details). In that model, family members are ejected in a planar configuration, but the ejections are randomly delayed over many orbits of Haumea. With some simple modifications, we have adjusted the model to allow ejections on timescales of  $\sim 10^7$  yr. When the two are compared, the resulting distributions of family members are very similar. The characteristic "X" shape present in Figure 4 of Proudfoot & Ragozzine (2019) is still present, along with its unique correlation between semimajor axis, eccentricity, and inclination of family members.

The similarity of the two resulting dynamical distributions allows us to draw some conclusions on the viability of our model based on the Bayesian fitting results presented in Proudfoot & Ragozzine (2019). While it was found that the DEPI model produced very good fits to the data, it could only do so when the ejection directions were close to isotropic, with the fits clearly ruling out a planar ejection. This result, however, did not take into account mechanisms that would work to isotropize the ejection directions. One distinctly possible mechanism is the precession of Haumea's rotation axis. In a manner similar to the precession of Earth's equinoxes, Haumea's rotation axis could slowly change,

making ejections aligned with Haumea's equator appear more isotropic. Another mechanism is the ejection of moonlets by mutual scattering events, which also may widen the distribution of ejection directions among escaping material. This effect may be significantly enhanced when the eccentricities and inclinations of close-in, orbiting material are dynamically pumped by Haumea's nonspherical gravitational potential (Scheeres et al. 2000). While a complete model that simulates all of these effects has not been tested, our proposed model shows promising consistency with the current dynamical distribution of family members. Further investigations of this model should include detailed simulations of the ejection process matched against the family orbital elements.

## 5.4. Uncertainties

### 5.4.1. Effects of (De)hydration on Angular Momentum

In our calculations of Haumea's present-day angular momentum, we have assumed that its core had a uniform density. However, the hydration and subsequent partial dehydration of Haumea's core would have affected the MOI, with the dehydrated inner core effectively acting as a third layer in Equation (1). Because the inner core is denser, this would decrease our estimate of Haumea's present-day angular momentum. Here we assess the magnitude of this effect by comparing two analytical cases with Haumea's overall mass and the same mantle and outer core densities, but with one having a higher density in the innermost 12% of the core volume.

In case 1, we assume a shape almost identical to the nominal case of  $a = 1056$ ,  $b = 840$ , and  $c = 537$  km and an average density of  $2000 \text{ kg m}^{-3}$ . If we assume that the core has the density of hydrated rock,  $2700 \text{ kg m}^{-3}$ , and the mantle is pure ice with a density of  $921 \text{ kg m}^{-3}$ , then the core must make up a fraction of 61.10% of the volume and have a mean radius of 662.7 km. The pure ice mantle makes up the remaining 38.90% of the volume. Assuming core axis ratios of  $b_c/a_c = 0.816$  and  $c_c/a_c = 0.531$  (Table 4), the core axes must be  $a_c = 875.7$ ,  $b_c = 714.6$ , and  $c_c = 465.0$  km. The MOI is then

$$I = \frac{1}{5}(\rho_c - \rho_m) V_c(a_c^2 + b_c^2) + \frac{1}{5}\rho_m(V_c + V_m)(a^2 + b^2), \quad (6)$$

which for our chosen values yields  $I = 1.223 \times 10^{33} \text{ kg m}^2$ . If the period is set at 3.9155 hr, then  $\omega = 2\pi/3.9155 \text{ hr}$ , and  $J = 5.452 \times 10^{29} \text{ kg m}^2 \text{ s}^{-1}$ . Our parameters are similar to the first entry in Table 1, which had a similar angular momentum of  $5.75 \times 10^{29} \text{ kg m}^2 \text{ s}^{-1}$ , but for ease of comparison, we will only compare the calculated value of  $J$  for the hypothetical case 1 to the three-layer case, case 2.

In case 2, we hold all values and assumptions of case 1 with the major exception of the inclusion of a dehydrated "inner core" with a density of  $3820 \text{ kg m}^{-3}$ . From the geochemical modeling performed in Section 4, we use the average core density of  $2890 \text{ kg m}^{-3}$  to calculate that the dehydrated inner core accounts for 17% of the core's total volume. This change also lowers the core volume fraction from 61.10% to 56.60%. This means the inner core is 7.16% of Haumea's total volume, the outer hydrated core is 49.44%, and the mantle is 43.40%. Keeping the mean radius of Haumea at 780.9 km fixes the inner

core’s mean radius at 324.3 km and the outer core’s mean radius at 646.0 km. The inner core would then have a total mass of  $0.546 \times 10^{21}$  kg (13.6% of the total), the outer core would have a mass of  $2.663 \times 10^{21}$  kg (66.5% of the total), and the ice mantle would have a mass of  $0.797 \times 10^{21}$  kg (19.9% of the total). We again assume the core axis ratios of case 1 because we seek a direct comparison and the numbers are reasonable to use, and we apply these ratios to both the inner and outer cores. This yields inner core axes of  $a_{ic} = 428.6$ ,  $b_{ic} = 349.7$ , and  $c_{ic} = 227.6$  km and outer core axes of  $a_c = 853.7$ ,  $b_c = 696.6$ , and  $c_c = 453.3$  km. Now the equation for MOI is

$$I = \frac{1}{5}(\rho_{ic} - \rho_{oc}) V_{ic}(a_{ic}^2 + b_{ic}^2) + \frac{1}{5}(\rho_{oc} - \rho_m)(V_{ic} + V_{oc})(a_{oc}^2 + b_{oc}^2) + \frac{1}{5}\rho_m V_{total}(a^2 + b^2), \quad (7)$$

where the subscript “ic” refers to the inner core, “oc” refers to the outer core, and “m” refers to the mantle. For our assumed values,  $I = 1.167 \times 10^{33}$  kg m<sup>2</sup>. Multiplying again by  $\omega = 2\pi/3.9155$  hr,  $J = 5.202 \times 10^{29}$  kg m<sup>2</sup> s<sup>-1</sup>. This is only 4.6% lower than the case 1 value.

If modern Haumea does have a dehydrated inner core, then this comparison suggests that we have overestimated Haumea’s angular momentum by assuming a uniform-density core. If the present-day angular momentum of Haumea is defined to be 4.6% lower than the two-layer solution with  $J = 5.75 \times 10^{29}$  kg m<sup>2</sup> s<sup>-1</sup>, then  $J_H = 5.49 \times 10^{29}$  kg m<sup>2</sup> s<sup>-1</sup>. A loss of 3% of pre-fling Haumea’s mass would then be completely consistent with the loss of 14% of the angular momentum, matching the modern value. Thus, a dehydrated inner core in Haumea may not only be supported by geochemical modeling but appears more consistent with the geophysical modeling as well.

However, it is difficult to be more conclusive, as the uncertainties in the inputs are themselves on the order of a few percent. Estimates of the axis ratio  $b/a$  range from 0.86 (0.76–0.88; Lacerda & Jewitt 2007; Lacerda et al. 2008), to 0.75–0.80 (Rabinowitz et al. 2006), to  $\approx 0.80$  (Lockwood et al. 2014). The calculation did not include more sophisticated equations of state that take into account composition, hydration state, and self-compression. The latter effect could lead to percent variations in quantities. Finally, the relatively coarse numerical resolution of *kyushu* precluded an evaluation of all possible solutions for a rotating, triaxial ellipsoid in hydrostatic equilibrium and was limited by its numerical resolution to solutions accurate only to within a few percent. Nevertheless, the best solutions we found suggest that the angular momentum of Haumea today may be closer to  $5.5 \times 10^{29}$  kg m<sup>2</sup> s<sup>-1</sup>, consistent with partial dehydration of the core.

#### 5.4.2. Mass of the Haumeans

Another source of uncertainty arises from the amount of mass that we assumed was lost to create the Haumean family. We assumed that the mass of the ejected Haumeans as a result of mass shedding during the interior’s evolution was 3% of Haumea’s mass,  $0.03 M_H$ . This value does not include any mass lost during the initial giant impact. Predictions of how much mass should be shed by rotational fission are similar but somewhat

higher; Schlichting & Sari (2009) predicted that the shed mass spun off of proto-Haumea as it stabilized following a graze-and-merge collision would have been 4%–7%  $M_H$ , but that is a slightly different scenario. Therefore, instead of predicting this quantity, we fixed it to the observed mass of the family members.

The observed mass of the family members is subject to uncertainty. At present, 10 Haumean family members have been positively identified, with only a handful of candidates proposed. A recent study (Pike et al. 2020) examined the known Haumean family members and searched for others using the Outer Solar System Origins Survey (OSSOS) ensemble, which extends to an absolute limiting magnitude  $H_r < 9.5$  or an inferred diameter of  $\approx 90$  km. This study also extended the velocity dispersion restriction to  $\Delta v < 230$  m s<sup>-1</sup> rather than 140 m s<sup>-1</sup> to attempt to find more family members. Their analysis showed that the lack of small Haumean family members is not a result of observation bias, as the smallest identified Haumean has an  $H_r$  of 7.9, well within the capabilities of OSSOS. Furthermore, the shallow  $H_r$ -magnitude distribution slopes,  $\alpha$ , were best approximated by values ranging from 0.0 to 0.6 (though  $\alpha$  values up to 0.9 were explored). These estimates are consistent with previous inferences of an upper limit of  $\alpha < 0.4$  (Proudford & Ragozzine 2019) and  $\alpha = 0.44_{-0.08}^{+0.1}$  (Vilenius et al. 2018). Interestingly, the  $\alpha$  values found in all of these analyses favor a rotational fission origin for the Haumeans and presumably are consistent with our scenario. The value favored by Pike et al. (2020),  $\alpha \approx 0.3$ , implies that there are  $450_{-390}^{+720}$  Haumean family members with  $H_r < 9.5$  (95% confidence interval) that together comprise 3% of Haumea’s total mass, consistent with the 2.6% estimate of Vilenius et al. (2018), though the range of  $\alpha$  values corresponds to a mass range of 1.4% (for  $\alpha = 0.6$ ) and 8.9% (for  $\alpha = 0.0$ ). The favored estimate for the mass of the family members is between 2% and 5% of Haumea’s total mass (Pike et al. 2020).

We did not explore parameter space to find solutions for initial masses for Haumea across this range. However, we fully expect that solutions would likewise exist for pre-fling cases with  $M = 1.02 M_H$  (or  $1.05 M_H$ ) that would correspond to  $J = 1.09 J_H$  (or  $1.23 J_H$ ). We must defer this analysis to future work.

## 6. Conclusions

The origins of the Haumea system have been unclear since the dwarf planet was discovered, though there are many good hypotheses. The “graze-and-merge” scenario of Leinhardt et al. (2010) successfully explains the high angular momentum of Haumea and could, in principle, explain in detail the mass and low velocity dispersion of ejected ice fragments. The model of Schlichting & Sari (2009) suggests that material also could have been ejected by rotational fission promptly after the impact, forming Haumea’s satellites, ring system, and family members. The recent *N*-body simulations by Sumida et al. (2020) strengthen the case for the ring and satellites forming from material escaping by rotational fission. Likewise, Campo Bagatin et al. (2016) concluded, on the basis of which collisions are likely, that rotational fission models (which this model resembles) are more probable than other models. These models are successful except for a few details. One is that the surface materials of the impactors are not expected to be pure ice but rather undifferentiated crusts of a rock–ice mixture. A second detail is that an impact between large ( $>1000$  km)

KBOs at the needed impact velocity of  $\sim 0.9 \text{ km s}^{-1}$  is unlikely except during the dynamical instability associated with Neptune’s migration, but maintaining the dynamical coherence of the family members demands that they are not ejected until after Haumea has been emplaced in the scattered disk and Neptune has stopped migrating.

Here we have proposed a new hypothesis building on these previous models. We consider Haumea to have acquired its high angular momentum during a graze-and-merge giant impact, which also ejected about 6% of its mass as fragments, now unidentifiable; however, the observed Haumean family members were ejected during a later stage by a geophysically triggered process. Specifically, if the impactors had only begun to differentiate, Haumea would form mostly undifferentiated; as Haumea’s core grew and its MOI decreased, its spin rate increased, eventually leading to vanishing effective gravity on the long ( $a$ ) axis. Material was flung off to become Haumea’s ring, moons, and dynamical family, carrying away about 3% of Haumea’s mass and 14% of its angular momentum. As the core hydrated and grew in size, the MOI increased again, and Haumea spun down to its present state. This model predicts that the ejection of the Haumeans occurred roughly 80 Myr after the giant impact, allowing the impact to happen during the dynamical instability but the ejection to occur after Haumea was in the scattered disk.

We tested the feasibility of this expanded hypothesis by calculating the possible internal structures a fluid Haumea in hydrostatic equilibrium could have had at key points in its history according to our proposed evolution using the *kyushu* code (Dunham et al. 2019). We calculated its mass and angular momentum and the size and density of its core, seeking solutions that offered continuity between stages. We found an analytical solution for a uniform-density Jacobi ellipsoid approximating Haumea immediately postimpact, with mass  $M = 1.03 M_H$  and angular momentum  $J = 1.14 J_H$ ; this matches a fully differentiated pre-fling calculated solution with the same mass and angular momentum, with a core density of  $3724 \text{ kg m}^{-3}$ , mass of  $3.25 \times 10^{21} \text{ kg}$ , and core–mantle boundary pressure  $P_{\text{CMB}} = 53 \text{ MPa}$ . We found a calculated post-fling fully differentiated solution with mass  $M = 1.00 M_H$  and angular momentum  $1.01 J_H$ , with a core density of  $3625 \text{ kg m}^{-3}$ , mass of  $3.16 \times 10^{21} \text{ kg}$ , and core–mantle boundary pressure  $P_{\text{CMB}} = 51 \text{ MPa}$ . To within the computational uncertainties of the problem, these core properties match, showing that Haumea could lose the required amount of angular momentum  $\delta J = 4.6(\delta M/M_H) J_H$  by losing the required amount of mass from the tip of the  $a$ -axis, maintaining the same internal structure. The average density of the post-fling solution,  $2049 \text{ kg m}^{-3}$ , is 4.5% higher than the average density of the pre-fling solution,  $1960 \text{ kg m}^{-3}$ , within the uncertainties of the expected increase in density by 3.5% due to the loss of  $0.03 M_H$  of pure ice. Finally, we confirmed the solution of Dunham et al. (2019) for present-day Haumea, favoring a similar set of parameters with  $a = 1056$ ,  $b = 840$ , and  $c = 537 \text{ km}$  and an average density of  $2008 \text{ kg m}^{-3}$ , with mass  $M = 1.00 M_H$ . This solution has a uniform core density of  $2697 \text{ kg m}^{-3}$  and mass of  $3.37 \times 10^{21} \text{ kg}$  due to the hydration of the core. Assuming a fully hydrated, uniform-density core, the angular momentum of Haumea would be  $1.05 J_H$ .

We used the *IcyDwarf* (Neveu et al. 2015a) code to calculate likely thermal and geochemical histories of Haumea. We found that Haumea’s core should be partially dehydrated,

yielding a slightly lower MOI and suggesting that Haumea’s present-day angular momentum is  $J = 1.00 J_H$ , where  $J_H \equiv 5.49 \times 10^{29} \text{ kg m}^2 \text{ s}^{-1}$ . Our thermal evolution calculations suggest that the full differentiation of the core and the flinging of ice from Haumea’s surface took place about 70–80 Myr after Haumea’s formation following the giant impact. We also predict that the hydration of the core commenced about 130–140 Myr after that, and that a subsurface ocean existed for about 250 Myr afterward.

We presented arguments that the giant impact that gave Haumea its large angular momentum occurred during the dynamical instability and Neptune’s migration, so that a collision was likely but the collisional fragments could be scattered by Neptune’s continued migration and Haumea removed to the scattered disk. Based on the need to match other constraints, we constrain the initiation of the instability to have occurred at about  $t = 55\text{--}60 \text{ Myr}$ , and we construct the following timeline for events in the early solar system (Table 5).

The synthesis of geophysical and thermal evolution modeling, along with details about the dynamical evolution of the solar system, allows a more detailed timeline than could be obtained using only one line of evidence at a time.

Our hypothesis does imply that Haumea was already in the scattered disk and Neptune had stopped migrating by the time the Haumeans were ejected. The ejection of material from the long  $a$ -axis of Haumea would be equivalent to planar ejection, which was ruled out by Proudfoot & Ragozzine (2019). However, an important distinction is that the geophysically driven ejection of the Haumeans means they would have been ejected over a span of  $\sim 10^7 \text{ yr}$ . Over that length of time, it is possible that Haumea’s pole could have precessed or moonlets could have scattered off each other, making the ejection trajectories of the family members somewhat more isotropic than planar, potentially resolving the discrepancy.

The need for the thermal evolution to match the details of the geophysical modeling (e.g., collapse of porosity, specific mineral densities) constrains Haumea’s properties. Our geochemical models show that Haumea was able to generate and sustain a liquid water ocean from 130 to 380 Myr postformation, a 250 Myr period. Haumea could indeed be an ancient potential ocean world of the solar system, the most distant one known. This may have grand implications for the search for habitability in the solar system and beyond, as an understanding of life’s physical limits is determined by the environments in which it can survive. In addition to the potential importance for ocean world studies, constraining the evolution and timescale of Haumea puts limits on events that involved the outer solar system, particularly Neptune’s migration. Future work will explore these scenarios more fully and evaluate how well dynamical predictions align with the timing of events described here.

We thank Emilie Dunham for a useful conversation that sparked many of the ideas presented here. We thank Sue Selkirk, who made the art of Haumea’s formation. We thank the anonymous reviewers for their thoughtful comments and feedback, as well as the journal managers and editor, Dr. Edgard Rivera-Valentín. Finally, we thank Darin Ragozzine for the discussions about Haumea’s formation and the light-curve analyses. This work was supported by grant 80NSSC19K0028 from NASA Solar System Workings (PI: Steve Desch). M.N.



acknowledges support from NASA under the CRESST II Cooperative Agreement (award No. 80GSFC21M0002). J.L. N.'s research was supported by an appointment to the NASA Postdoctoral Program at Goddard Space Flight Center, administered by Oak Ridge Associated Universities under contract with NASA. The views and conclusions contained in this document are those of the authors and should not be interpreted as representing the official policies, either expressed or implied, of the National Aeronautics and Space Administration (NASA) or the US Government. The US Government is authorized to reproduce and distribute reprints for government purposes notwithstanding any copyright notation herein.

### Appendix

Here we present additional results obtained using the *kyushu* code that include variations in the *a*- and *b*-axes. In Figures 6, 7, and 8, we plot the variations in the *c*-axis, average density  $\rho_{\text{avg}}$ , and core density  $\rho_c$  that correspond to solutions in hydrostatic equilibrium for Haumea's modern mass  $M_H = 4.006 \times 10^{21}$  kg and rotation period of 3.915 hr, assuming the mantle density is that of ice,  $921 \text{ kg m}^{-3}$ . In Table 6 and Figure 9, we show the solutions for the case of the pre-fling Haumea, with a mass of  $1.03 M_H$  and mantle density of  $921 \text{ kg m}^{-3}$ . For these simulations, the rotation period was not imposed.

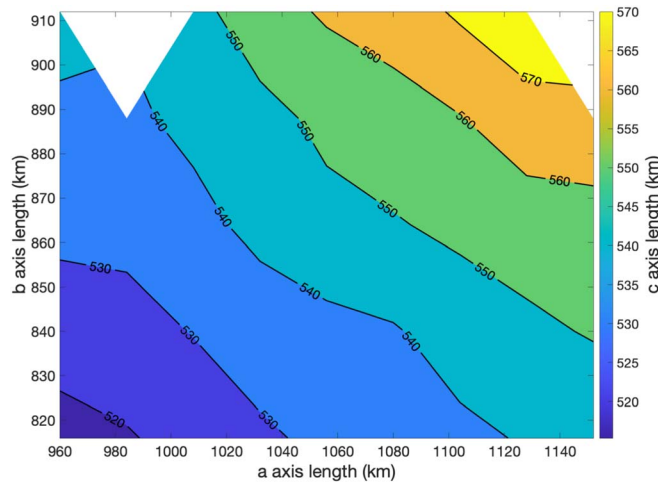


Figure 6. Length of *c*-axis as a function of axes *a* and *b*.

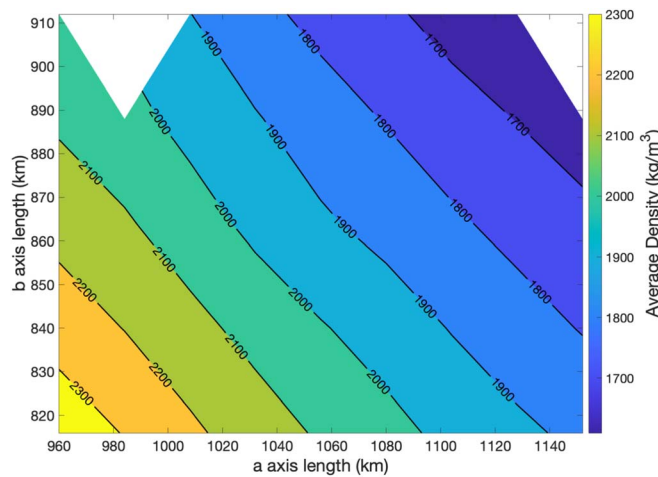
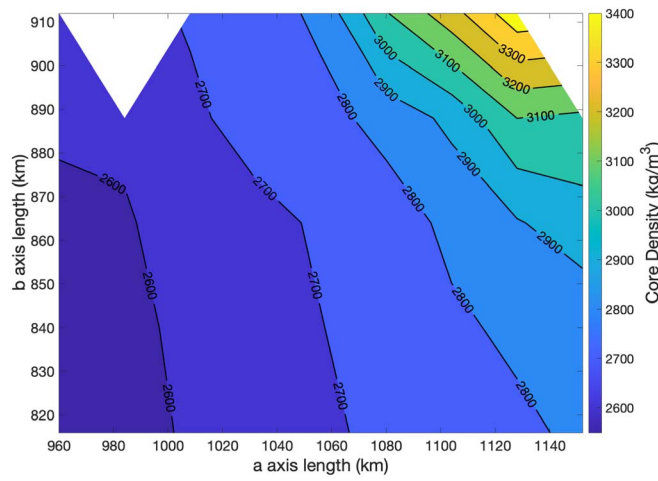


Figure 7. Average density  $\rho_{\text{avg}}$  as a function of axes *a* and *b*.



**Figure 8.** Core density  $\rho_c$  as a function of axes  $a$  and  $b$ .

**Table 6**  
All Modeled Solutions for a Pre-fling Haumea with Mass  $M = 1.03 M_H$

| Case No. | $\rho_m$<br>( $\text{kg m}^{-3}$ ) | $P$<br>(hr)  | $a$<br>(km) | $b$<br>(km) | $c$<br>(km)  | $\bar{\rho}$<br>( $\text{kg m}^{-3}$ ) | $a_c$<br>(km) | $b_c$<br>(km) | $c_c$<br>(km) | $\rho_c$<br>( $\text{kg m}^{-3}$ ) | $M_c$<br>( $10^{21}$ kg) | $g_{\text{eff}}$<br>( $\text{m s}^{-2}$ ) | $J$<br>( $10^{29}$ $\text{kg m}^2 \text{s}^{-1}$ ) |
|----------|------------------------------------|--------------|-------------|-------------|--------------|--|---------------|---------------|---------------|------------------------------------|--------------------------|---|--|
| 9        | 921                                | 3.601        | 1056        | 840         | 530.6        | 2093                                   | 804           | 678           | 444           | 3296                               | 3.34                     | 0.342 6                                   | 5.79   |
| 10       | 921                                | 3.525        | 1056        | 840         | 527.4        | 2106                                   | 780           | 666           | 438           | 3469                               | 3.31                     | 0.079 6                                   | 5.78   |
| 11       | 921                                | 3.400        | 1056        | 840         | 526.2        | 2110                                   | 720           | 642           | 426           | 3921                               | 3.23                     | 0.037 8                                   | 5.73   |
| 12       | 921                                | 3.700        | 1056        | 840         | 533.0        | 2083                                   | 834           | 696           | 456           | 3062                               | 3.40                     | 0.113 0                                   | 5.78   |
| 13       | 921                                | 3.790        | 1056        | 840         | 534.3        | 2078                                   | 870           | 714           | 462           | 2862                               | 3.44                     | 0.131 0                                   | 5.79   |
| 14       | 921                                | 3.924        | 1056        | 840         | 542.0        | 2049                                   | 900           | 726           | 480           | 2666                               | 3.50                     | 0.151 0                                   | 5.73   |
| 15       | 921                                | 3.421        | 1080        | 840         | 530.2        | 2048                                   | 720           | 636           | 432           | 3913                               | 3.24                     | 0.019 0                                   | 5.88   |
| 16       | <i>921</i>                         | <i>3.393</i> | <i>1104</i> | <i>840</i>  | <i>528.3</i> | <i>2011</i>                            | <i>714</i>    | <i>636</i>    | <i>426</i>    | <i>3976</i>                        | <i>3.22</i>              | <i>-0.0276</i>                            | <i>6.07</i>  |
| 17       | 921                                | 3.520        | 1104        | 840         | 532.6        | 1994                                   | 756           | 648           | 432           | 3611                               | 3.20                     | 0.031 7                                   | 5.98   |
| 18       | <i>921</i>                         | <i>3.417</i> | <i>1128</i> | <i>840</i>  | <i>526.8</i> | <i>1973</i>                            | <i>732</i>    | <i>642</i>    | <i>432</i>    | <i>3858</i>                        | <i>3.28</i>              | <i>-0.0371</i>                            | <i>6.31</i>  |
| 19       | 921                                | 4.602        | 1152        | 840         | 566.4        | 1797                                   | 1104          | 804           | 546           | 1911                               | 3.88                     | 0.180 4                                   | 6.10   |
| 20       | 921                                |              | 1056        | 864         |              |  |               |               |               |                                    | No solution found        |   |  |
| 21       | 921                                | 3.498        | 1056        | 864         | 532.2        | 2029                                   | 738           | 660           | 432           | 3638                               | 3.12                     | 0.064 8                                   | 5.82   |
| 22       | 921                                | 3.583        | 1056        | 864         | 536.5        | 2012                                   | 768           | 672           | 438           | 3402                               | 3.22                     | 0.083 5                                   | 5.81   |
| 23       | 921                                | 3.699        | 1056        | 864         | 538.7        | 2004                                   | 810           | 696           | 450           | 3095                               | 3.29                     | 0.105 0                                   | 5.82   |
| 24       | 921                                | 3.811        | 1056        | 864         | 543.9        | 1985                                   | 840           | 708           | 462           | 2890                               | 3.33                     | 0.124 0                                   | 5.77   |
| 25       | 921                                | 3.914        | 1056        | 864         | 548.0        | 1970                                   | 870           | 726           | 474           | 2699                               | 3.38                     | 0.139 9                                   | 5.76   |
| 26       | 921                                | 3.528        | 1080        | 840         | 531.4        | 2043                                   | 768           | 654           | 438           | 3542                               | 3.26                     | 0.057 8                                   | 5.88   |
| 27       | 921                                | 3.571        | 1080        | 840         | 530.5        | 2047                                   | 786           | 666           | 438           | 3395                               | 3.26                     | 0.067 2                                   | 5.86   |
| 28       | 921                                | 3.801        | 1080        | 840         | 536.8        | 2023                                   | 828           | 684           | 450           | 3113                               | 3.32                     | 0.093 6                                   | 5.86   |
| 29       | 921                                | 3.814        | 1080        | 840         | 541.2        | 2006                                   | 858           | 696           | 462           | 2892                               | 3.34                     | 0.113 0                                   | 5.79   |
| 30       | 921                                | 3.906        | 1080        | 840         | 544.4        | 1995                                   | 888           | 714           | 474           | 2729                               | 3.44                     | 0.128 0                                   | 5.83   |
| 31       | 921                                |              | 1080        | 864         |              |  |               |               |               |                                    | No solution found        |   |  |
| 32       | 921                                | 3.501        | 1080        | 864         | 538.5        | 1962                                   | 720           | 642           | 432           | 3767                               | 3.15                     | 0.038 2                                   | 5.90   |
| 33       | 921                                | 3.603        | 1080        | 864         | 541.0        | 1955                                   | 762           | 660           | 438           | 3435                               | 3.17                     | 0.066 8                                   | 5.89   |
| 34       | 921                                | 3.721        | 1080        | 864         | 544.9        | 1937                                   | 798           | 678           | 450           | 3144                               | 3.21                     | 0.089 0                                   | 5.85   |
| 35       | 921                                | 3.801        | 1080        | 864         | 547.9        | 1927                                   | 822           | 696           | 456           | 2959                               | 3.23                     | 0.102 7                                   | 5.84   |
| 36       | 921                                | 3.891        | 1080        | 864         | 548.3        | 1925                                   | 858           | 714           | 468           | 2756                               | 3.31                     | 0.117 9                                   | 5.85   |
| 37       | 921                                | 3.605        | 1104        | 840         | 535.5        | 1984                                   | 786           | 660           | 438           | 3380                               | 3.22                     | 0.053 0                                   | 5.96   |
| 38       | 921                                | 3.716        | 1104        | 840         | 540.6        | 1965                                   | 822           | 672           | 450           | 3133                               | 3.26                     | 0.075 1                                   | 5.94   |
| 39       | 921                                | 3.801        | 1104        | 840         | 543.0        | 1956                                   | 846           | 684           | 456           | 2961                               | 3.27                     | 0.091 9                                   | 5.88   |
| 40       | 921                                | 3.903        | 1104        | 840         | 545.1        | 1949                                   | 882           | 702           | 468           | 2762                               | 3.35                     | 0.110 1                                   | 5.90   |
| 41       | <i>921</i>                         | <i>3.475</i> | <i>1128</i> | <i>840</i>  | <i>530.4</i> | <i>1960</i>                            | <i>744</i>    | <i>648</i>    | <i>432</i>    | <i>3724</i>                        | <i>3.25</i>              | <i>-0.0143</i>                            | <i>6.24</i>  |

**Note.** The code was unable to find stable solutions for two scenarios (20 and 31). Both of these had a larger  $b$ -axis and an input period of 3.4 hr, which suggests that there is a maximum size for each rotation rate for Haumea. Run 19 could not converge on a solution with an appropriate period for Haumea. The solutions that meet all of the criteria for possible early-stage Haumeas (16, 18, and 41) are italicized in this chart for easy identification. Estimated uncertainties in output quantities are  $\pm 3.3$  km ( $c$  semiaxis),  $\pm 12$   $\text{kg m}^{-3}$  (average density),  $\pm 70$   $\text{kg m}^{-3}$  (core density), and  $\pm 0.031$  hr (period).

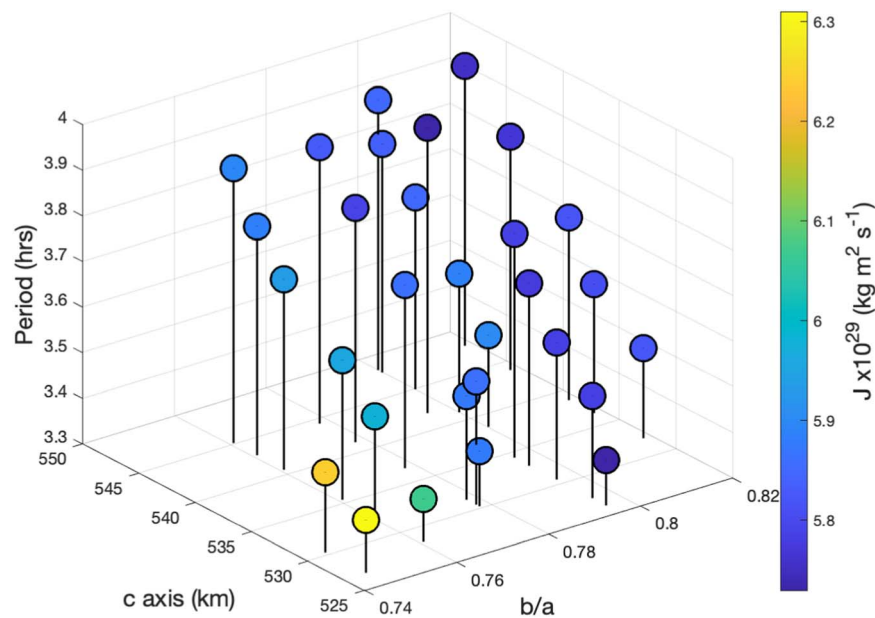


**Figure 9.** Visual representation of all of the pre-fling scenarios included in Table 5. The three cases with the lowest values of  $b/a$  and  $c$  are cases 16, 18, and 41.

### ORCID iDs

Jessica L. Noviello <https://orcid.org/0000-0001-5224-8807>  
 Steven J. Desch <https://orcid.org/0000-0002-1571-0836>  
 Marc Neveu <https://orcid.org/0000-0002-6220-2869>  
 Benjamin C. N. Proudfoot <https://orcid.org/0000-0002-1788-870X>  
 Sarah Sonnett <https://orcid.org/0000-0003-2762-8909>

### References

- Barboni, M., Boehnke, P., Keller, B., et al. 2017, *SciA*, **3**, e1602365  
 Barkume, K. M., Brown, M. E., & Schaller, E. L. 2006, *ApJL*, **640**, L87  
 Benz, W., & Asphaug, E. 1999, *Icar*, **142**, 5  
 Bierson, C. J., & Nimmo, F. 2019, *Icar*, **326**, 10  
 Bierson, C. J., Nimmo, F., & Stern, S. A. 2020, *NatGe*, **13**, 468  
 Brown, M. E., Barkume, K. M., Ragozzine, D., & Schaller, E. L. 2007, *Natur*, **446**, 294  
 Brownlee, D., Tsou, P., Aléon, J., et al. 2006, *Sci*, **314**, 1711  
 Campo Bagatin, A., Benavidez, P. G., Ortiz, J. L., & Gil-Hutton, R. 2016, *MNRAS*, **461**, 2060  
 Canup, R. M. 2005, *Sci*, **307**, 546  
 Chandrasekhar, S. 1969, *Commun. Pure Appl. Math.*, **20**, 251  
 de Sousa, R. R., Morbidelli, A., Raymond, S. N., et al. 2020, *Icar*, **339**, 113605  
 Desch, S. J., Cook, J. C., Doggett, T. C., & Porter, S. B. 2009, *Icar*, **202**, 694  
 Desch, S. J., & Neveu, M. 2015, *LPSC*, **46**, 2082  
 DeSouza, S. R., Roig, F., & Nesvorný, D. 2021, *MNRAS*, **507**, 539  
 Dunham, E. T., Desch, S. J., & Probst, L. 2019, *ApJ*, **877**, 41  
 Durham, W. B., McKinnon, W. B., & Stern, L. A. 2005, *GeoRL*, **32**, L18202  
 Fulle, M., Della Corte, V., Rotundi, A., et al. 2016, *MNRAS*, **462**, S132  
 Fulle, M., Della Corte, V., Rotundi, A., et al. 2017, *MNRAS*, **469**, S45  
 Gourgeot, F., Carry, B., Dumas, C., et al. 2016, *A&A*, **593**, A19  
 Hachisu, I. 1986a, *ApJS*, **61**, 479  
 Hachisu, I. 1986b, *ApJS*, **62**, 461  
 Holsapple, K. A. 2001, *Icar*, **154**, 432  
 Huang, P.-W., & Wellmann, F. 2021, *Transport in Porous Media*, **137**, 195  
 Jewitt, D., Weaver, H., Agarwal, J., Mutchler, M., & Drahus, M. 2010, *Natur*, **467**, 117  
 Kondratyev, B. P. 2016, *Ap&SS*, **361**, 169  
 Kondratyev, B. P., & Kornoukhov, V. S. 2018, *MNRAS*, **478**, 3159  
 Lacerda, P., Jewitt, D., & Peixinho, N. 2008, *AJ*, **135**, 1749  
 Lacerda, P., & Jewitt, D. C. 2007, *AJ*, **133**, 1393  
 Leinhardt, Z. M., Marcus, R. A., & Stewart, S. T. 2010, *ApJ*, **714**, 1789  
 Leinhardt, Z. M., & Stewart, S. T. 2012, *ApJ*, **745**, 79  
 Lellouch, E., Kiss, C., Santos-Sanz, P., et al. 2010, *A&A*, **518**, L147  
 Levison, H. F., Morbidelli, A., Vokrouhlický, D., & Bottke, W. F. 2008, *AJ*, **136**, 1079  
 Lockwood, A. C., Brown, M. E., & Stansberry, J. 2014, *EM&P*, **111**, 127  
 Macdonald, A., & Fyfe, W. 1985, *Tectonophysics*, **116**, 123  
 Macke, R. J., Consolmagno, G. J., & Britt, D. T. 2011, *M&PS*, **46**, 1842  
 Malamud, U., & Prialnik, D. 2015, *Icar*, **246**, 21  
 Malhotra, R. 1993, *Natur*, **365**, 819  
 McKinnon, W. B., Stern, S. A., Weaver, H. A., et al. 2017, *Icar*, **287**, 2  
 Nesvorný, D., & Vokrouhlický, D. 2016, *ApJ*, **825**, 94  
 Nesvorný, D., Vokrouhlický, D., Bottke, W. F., & Levison, H. F. 2018, *NatAs*, **2**, 878  
 Neveu, M., Desch, S. J., & Castillo-Rogez, J. C. 2015a, *JGRE*, **120**, 123  
 Neveu, M., Desch, S. J., Shock, E. L., & Glein, C. R. 2015b, *Icar*, **246**, 48  
 Ortiz, J. L., Santos-Sanz, P., Sicardy, B., et al. 2017, *Natur*, **550**, 219  
 Ortiz, J. L., Thirouin, A., Campo Bagatin, A., et al. 2012, *MNRAS*, **419**, 2315  
 Pike, R. E., Proudfoot, B. C. N., Ragozzine, D., et al. 2020, *NatAs*, **4**, 89  
 Pinilla-Alonso, N., Brunetto, R., Licandro, J., et al. 2009, *A&A*, **496**, 547  
 Price, E. M., & Rogers, L. A. 2020, *ApJ*, **894**, 8  
 Proudfoot, B. C. N., & Ragozzine, D. 2019, *AJ*, **157**, 230  
 Rabinowitz, D. L., Barkume, K., Brown, M. E., et al. 2006, *ApJ*, **639**, 1238  
 Ragozzine, D., & Brown, M. E. 2007, *AJ*, **134**, 2160  
 Ragozzine, D., & Brown, M. E. 2009, *AJ*, **137**, 4766  
 Scheeres, D. J. 1994, *Icar*, **110**, 225  
 Scheeres, D. J., Williams, B. G., & Miller, J. K. 2000, *JGCD*, **23**, 466  
 Schlichting, H. E., & Sari, R. 2009, *ApJ*, **700**, 1242  
 Sharp, T. G., & de Carli, P. S. 2006, in *Meteorites and the Early Solar System II*, ed. D. S. Lauretta & H. Y. McSween (Tucson, AZ: Univ. Arizona Press), **653**  
 Sumida, I., Ishizawa, Y., Hosono, N., & Sasaki, T. 2020, *ApJ*, **897**, 21  
 Tsiganis, K., Gomes, R., Morbidelli, A., & Levison, H. F. 2005, *Natur*, **435**, 459  
 Vilenius, E., Stansberry, J., Müller, T., et al. 2018, *A&A*, **618**, A136  
 Volk, K., & Malhotra, R. 2012, *Icar*, **221**, 106  
 Wasson, J. T., & Kallemeyn, G. W. 1988, *RSPTA*, **325**, 535  
 Weisberg, M. K., McCoy, T. J., & Krot, A. N. 2006, in *Meteorites and the Early Solar System II*, ed. D. S. Lauretta & H. Y. McSween (Tucson, AZ: Univ. Arizona Press), **19**  
 Yasui, M., & Arakawa, M. 2009, *JGRE*, **114**, E09004